

FILE COPY

Naval Research Laboratory

Washington, DC 20375-5000



2

NRL Memorandum Report 6714

AD-A227 522

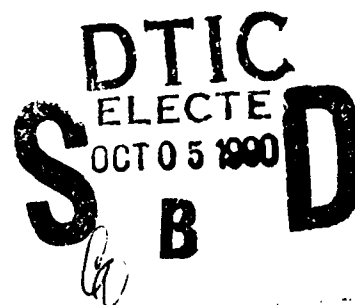
Superresolution Techniques and ISAR Imaging

WILLIAM F. GABRIEL*

*Radar Analysis Branch
Radar Division*

**SFA, Inc.
Landover, MD 20785*

September 21, 1990



Approved for public release; distribution unlimited.

REPORT DOCUMENTATION PAGE			Form Approved OMB No. 0704-0188	
Public reporting burden for this collection of information is estimated to average 1 hour per response, including the time for reviewing instructions, searching existing data sources, gathering and maintaining the data needed, and completing and reviewing the collection of information. Send comments regarding this burden estimate or any other aspect of this collection of information, including suggestions for reducing this burden, to Washington Headquarters Services, Directorate for Information Operations and Reports, 1215 Jefferson Davis Highway, Suite 1204, Arlington, VA 22202-4302, and to the Office of Management and Budget, Paperwork Reduction Project (0704-0188), Washington, DC 20503.				
1. AGENCY USE ONLY (Leave blank)	2. REPORT DATE 1990 September 21	3. REPORT TYPE AND DATES COVERED Interim Oct 87 - Oct 89		
4. TITLE AND SUBTITLE SUPERRESOLUTION TECHNIQUES AND ISAR IMAGING		5. FUNDING NUMBERS PE - ONT RA11W51		
6. AUTHOR(S) William F. Gabriel*				
7. PERFORMING ORGANIZATION NAME(S) AND ADDRESS(ES) Naval Research Laboratory Washington, DC 20375-5000		8. PERFORMING ORGANIZATION REPORT NUMBER NRL Memorandum Report 6714		
9. SPONSORING / MONITORING AGENCY NAME(S) AND ADDRESS(ES) Office of Naval Technology Arlington, VA 22217		10. SPONSORING / MONITORING AGENCY REPORT NUMBER		
11. SUPPLEMENTARY NOTES *SFA, Inc., Landover, MD 20785				
12a. DISTRIBUTION / AVAILABILITY STATEMENT Approved for public release; distribution unlimited			12b. DISTRIBUTION CODE	
13. ABSTRACT (Maximum 200 words) <p>High-resolution optimal estimation techniques have been applied to the problem area of radar imaging of rotating objects. Typical digital range-Doppler processor operations are described, utilizing several of the many superresolution techniques available in the literature. Their application to the range domain represents new R&D work, wherein multiple scatterers within one range bin have been resolved without increasing the bandwidth. Simulation results show the feasibility for achieving superresolution in the Doppler domain only, the range domain only, or both domains jointly in a three-dimensional (3D) processed image.</p> <p>The capability for focusing upon a small section of the overall image and achieving finer detail (magnification) should be particularly useful. It is concluded that superresolution techniques offer a valuable complement to conventional DFT-ISAR image processing, and should permit either higher resolution images from the same data samples, or equal quality images from significantly fewer data samples. The reader is cautioned that these techniques are not applicable in certain situations where "total coherence" exists over the entire observation interval. (RH)</p>				
14. SUBJECT TERMS ISAR IMAGING Radar Imaging Superresolution Imaging Adaptive pulse compression Target resolution			15. NUMBER OF PAGES 65	
			16. PRICE CODE	
17. SECURITY CLASSIFICATION OF REPORT UNCLASSIFIED	18. SECURITY CLASSIFICATION OF THIS PAGE UNCLASSIFIED	19. SECURITY CLASSIFICATION OF ABSTRACT UNCLASSIFIED	20. LIMITATION OF ABSTRACT SAR	

CONTENTS

1. INTRODUCTION	1
2. DOPPLER DOMAIN PROCESSING ALGORITHMS	2
Discrete Fourier Transform (DFT)	4
Howells-Applebaum (H-A) Algorithm	6
Sample Matrix Inverse (SMI) Algorithm	7
Maximum Likelihood Method (MLM) Algorithm	8
"Beamspace" LPF Algorithm	9
3. SIMULATED DATA RESULTS	10
Rotating Boom Model	10
Targets Entering/Leaving a Rangebin	14
Merry-go-round Model	16
4. RANGE DOMAIN SUPERRESOLUTION	18
Matched Filter DFT	20
MLM Algorithm	23
SLC Algorithm	25
Coherent Target Scatterers	25
Simulated Data Results	27
5. COMBINED RANGE/DOPPLER 3D SUPERRESOLUTION IMAGING	29
Conventional Fourier Transform	30
MLM/LPF Algorithms	31
Digital Image from Optimum Weight Roots	32
Triangle Model of Ten Point-targets	33
Triangle Model with Coherence Present	35
6. CONCLUSIONS	36
REFERENCES	37

Accession For	
NTIS GRA&I	<input checked="" type="checkbox"/>
DTIC TAB	<input type="checkbox"/>
Unannounced	<input type="checkbox"/>
Justification	
By _____	
Distribution/	
Availability Codes	
Dist	Avail and/or Special
A-1	

SUPERRESOLUTION TECHNIQUES AND ISAR IMAGING

1. INTRODUCTION

Radar imaging of rotating objects has been an area of interest for more than a decade, and several descriptions of the techniques/systems involved are available in the literature [1-5]. Essentially, such a system consists of a high-quality, coherent, pulse doppler radar feeding its received signals into a suitable range-Doppler processor. If digital processing is desired, the radar receiver output is down-converted in a synchronous detector to baseband video I+Q (in-phase and quadrature) signals and sampled with A/D (analogue-to-digital) converters. Digital range-Doppler processing may then be carried out in convenient discrete Fourier transform (DFT) devices. The resolution capabilities of these systems are based upon the well-known principles of the conventional windowed Fourier transform both in the Doppler domain and the range domain. The rotation of the object field relative to the radar generates a Doppler frequency gradient and permits the extraction of cross-range resolution that is much finer than that obtainable by the radar's antenna beamwidth.

This paper describes an investigation wherein high-resolution optimal estimation techniques are applied to the radar imaging problem area. These methods, sometimes referred to as "Superresolution" techniques [6], are a current technology that is of considerable interest because of resolution capabilities that extend well beyond the conventional windowed Fourier transform. They have been successfully applied in spectral analysis, seismic arrays, RF spatial arrays, and MTI doppler filters [7-11]. Thus, it is natural to consider their application to ISAR (Inverse Synthetic Array Radar)

Manuscript approved July 6, 1990.

imaging, in the hope that one could obtain either higher resolution images from the same data samples, or equal-quality images from significantly fewer data samples.

2. Doppler Domain Processing Algorithms

In this section, we assume an input from the radar receiver consisting of conventional range data samples occurring at the usual Nyquist sampling rate, f_s , which is equal to the IF receiver bandwidth. If the radar utilizes a pulse compression waveform, then the sampling is performed after the pulse compression filter. The spacing of the samples in the time domain is the reciprocal of f_s and defines a "rangebin" for the purposes of this discussion. Furthermore, we assume that a selectable "range window" of adjacent rangebin data samples is available from each prf, and that there exists within this window a prominent point-target scatterer which serves as a range reference tracking point, i.e., the range window is referenced to some point on the target and tracks/moves with it. The acquisition and tracking of this reference point is crucial to achieving high resolution in two-dimensional target imaging, because it is utilized for automatic/adaptive self-calibration of the system [12]. This reference point is sometimes referred to as a "dominant scatterer" on the target. Reference [12] is recommended for a tutorial discussion on the need for effective self-calibration and an adaptive technique that is capable of providing the necessary compensation.

In essence, the inverse synthetic array is "focused" upon the tracked dominant scatterer. Further information on target tracking systems may be found in [13].

The Doppler domain is approached from the viewpoint of a classical time domain transversal filter[13,14], as illustrated in Fig. 1. Here, we visualize feeding the above rangebin data samples into a tapped delay line wherein the inter-tap delay is precisely equal to the reciprocal of the prf. Thus, the sequence of range window data samples will be synchronized in time at every tap along the delay line. With this viewpoint in mind, consider forming a large digital-data storage matrix, \underline{D} , of dimension M rows by N columns, wherein the columns contain the adjacent rangebin data samples within our selected range window. Thus, a typical matrix element, D_{mn} , contains the m^{th} rangebin sample in the n^{th} prf period. As the data samples associated with each prf period come in, two matrix processing steps occur:

- a) The columns of \underline{D} are shifted to the left by one, with the oldest column ($n=1$) being bumped off (discarded).
- b) The new incoming data samples from the current prf are entered into the right-hand column ($n=N$).

Note that it requires N prf periods to initially fill the matrix \underline{D} . After all columns have been filled, via the above two steps, we can form a signal vector, $\underline{E}_m(k)$, for each rangebin row,

$$\underline{E}_m^t(k) = [E_{m1}(k), E_{m2}(k), E_{m3}(k), \dots, E_{mN}(k)] \quad (1)$$

where (k) denotes the k^{th} time sampling of the signal vector, subscript m denotes the m^{th} rangebin, the subscripts 1 through N denote the delay line taps, and superscript t denotes the transpose of the vector $\underline{E}_m(k)$.

The time domain signal vector represented by equation (1) may be processed via many different transversal filter algorithms to obtain Doppler domain spectra. Brief descriptions of a few such algorithms follow.

Discrete Fourier Transform (DFT)

The DFT is a Fourier representation of a finite-length sequence which is itself a sequence rather than a continuous function [15]. Not only is the DFT primary in conventional ISAR image processing, but it plays a central role in the implementation of a variety of digital signal processing algorithms, including some of the superresolution techniques. One of its implementations important to our purposes is the formulation of a frequency domain filter which will permit sampling at a selected Doppler frequency. Briefly, we multiply the signal vector of (1) with a filter vector weighted for the desired Doppler frequency, f ,

$$V_m(k, f) = \left[\underline{E}_m^t(k) \cdot \underline{W}(f) \right] = \sum_{n=1}^N E_{mn}(k) w_n(f) \quad (2)$$

where $V_m(k, f)$ is the k^{th} time sample at frequency f for the m^{th} rangebin.

$\underline{W}(f)$ is the filter vector at frequency f ,

$w_n(f)$ is the n^{th} tap weight of $\underline{W}(f)$.

Equation (2) essentially defines a "beamformer" as illustrated in Fig. 2. The individual weights are readily computed from the phase gradient along the delay line taps for frequency f ,

$$w_n(f) = \frac{1}{\sqrt{N}} \exp[j\omega(N-n)] \quad (3)$$

$$\text{where } \omega = 2\pi \left(\frac{f}{\text{prf}} \right) \text{ radians} \quad (4)$$

Uniform amplitude weighting is employed in (3) and it will result in a $(\sin x)/x$ type of filter response. Tapered amplitude weighting is an option, of course.

Note in equation (4) that Doppler frequency, f , is normalized to the prf such that our normalized angular frequency, ω , will be in radians with a range of $-\pi \leq \omega \leq \pi$ under normal Nyquist sampling assumptions [15].

A second DFT implementation utilized in our processing is to form a multiple set of $(\sin x)/x$ Doppler filters that satisfy orthogonal separation criteria. This becomes equivalent to a digital Fast Fourier Transform, (FFT) [15] and has an exact correspondence to the Butler matrix spatial beamformer [16]. The complete transformation matrix, \underline{B} , consists of N column vectors of N tap weights. A typical matrix element weight, b_{nl} , is of the form,

$$b_{nl} = \frac{1}{\sqrt{N}} \exp \left\{ -j \frac{2\pi}{N} \left[l - \left(\frac{N+1}{2} \right) \right] (N-n) \right\} \quad (5)$$

where l = Doppler frequency filter index

n = tap weight index

N = total number of taps

This transformation is utilized in the "beam-space" LPF algorithm.

A third DFT implementation, utilized for plotting the Doppler spectrum is to average the sampled power from (2) over K time samples,

$$P_m(f) = \frac{1}{K} \sum_{k=1}^K V_m^*(k,f) \cdot V_m(k,f) \quad (6)$$

where $P_m(f)$ is the Doppler spectrum power at frequency f , and the symbol $*$ denotes complex conjugate. Substituting into (6) from (2) we obtain,

$$P_m(f) = \underline{W}^*(f) \cdot \hat{\underline{R}}_m \cdot \underline{W}(f) \quad (7)$$

$$\text{where } \hat{\underline{R}}_m = \frac{1}{K} \sum_{k=1}^K \left[\underline{E}_m^*(k) \cdot \underline{E}_m^t(k) \right]. \quad (8)$$

$\hat{\underline{R}}_m$ is the familiar sample covariance matrix averaged over K updates [14]. Note that the total number of prf implied by (8) will be equal to the K updates plus the initial N prf required to fill the delay line.

Howells-Applebaum (H-A) Algorithm

This well-known adaptive array algorithm is popular in practical applications because it does not require data storage as in the sample covariance matrix, nor does it require a matrix inverse computation. It simply computes the cross-correlations between the array output and each tap signal, and integrates those updates into the N weights. Fig. 2 can serve as a schematic diagram if we consider the weights adaptive. A simple digital recursive version of this algorithm may be written per references [17,18],

$$T W_n(k+1) = (T-1)W_n(k) + S_n^*(f) - g E_{mn}^*(k) Y_o(k) \quad (9)$$

$$\text{where } Y_o(k) = \sum_{n=1}^N E_{mn}(k) W_n(k) \quad \text{is the array output} \quad (10)$$

$W_n(k+1)$ is the updated n^{th} tap adaptive weight,

$W_n(k)$ is the current n^{th} tap adaptive weight,

$E_{mn}(k)$ is the tap signal from equation (1),

$S_n^*(f)$ is a deterministic "steering" filter weight,

g is a gain parameter,

T is a weight integration parameter.

The H-A algorithm is a steepest-descent, feedback type of adaptive filter that attempts to drive the output toward white noise by moving filter zeros/nulls onto spectral lines within the incoming signal. It requires only $2N$ multiplies per update, and yet is capable of satisfactory adaptive filter performance for many applications. However, it does have certain performance limitations that should be evaluated [14].

Sample Matrix Inverse (SMI) Algorithm

The SMI algorithm computes an optimum Wiener filter adaptive weight from the inverse of the sample covariance matrix [14],

$$\underline{w}_o = \mu \hat{R}_m^{-1} \underline{s}^*(f) \quad (11)$$

where \underline{w}_o is the optimum filter weight vector,

$\underline{s}^*(f)$ is a "steering" filter vector at frequency f ,

μ is a scalar.

This algorithm is generally superior in performance to the H-A algorithm, but it also requires data storage in the sample covariance matrix and must compute the inverse. Approximately N^3 multiplies per update are required.

To ease the computer storage requirement in accumulating a total of M sample covariance matrices, it is expedient to store only the upper triangle of the Hermitian matrices, i.e.,

$$\text{accumulate } \hat{R}_m = \begin{bmatrix} r_{11} & r_{12} & r_{13} \\ & r_{22} & r_{23} \\ 0 & & r_{33} \end{bmatrix} \quad (12)$$

where $\underline{0}$ denotes a lower triangle matrix of zeros. When the $\hat{\underline{R}}_m$ have been completed, we then compute and inject a diagonal "psuedonoise" term, β_m^2 ,

$$s_m^2 = \sigma_0^2 + \alpha \sqrt{\frac{\sigma_0^2}{N} \text{Trace} \left(\hat{\underline{R}}_m \right)} \quad (13)$$

where σ_0^2 is the average noise power level per tap, and α is the psuedonoise magnitude factor.

The advantages of adding a small amount of psuedonoise are described in reference [9].

The next processing step then consists of inverting the M modified sample covariance matrices,

$$\hat{\underline{R}}_m^{-1} = \left[\hat{\underline{R}}_m + \beta_m^2 \underline{I} \right]^{-1} \quad (14)$$

where \underline{I} denotes the identity matrix, and substituting into (11) to obtain the optimum Wiener filter weights.

Maximum Likelihood Method (MLM) Algorithm

The MLM algorithm was introduced by Capon [6,7], and is defined as a filter designed to pass the power in a narrow band about the signal frequency of interest, and to minimize or reject all other frequency components in an optimal manner. Thus, our Doppler spectrum power may be estimated by substituting optimum Wiener filter weights from (11) into (7),

$$P_m(f) = \underline{W}_0^{*t} \cdot \hat{\underline{R}}_m^{-1} \cdot \underline{W}_0 \quad (15)$$

The MLM algorithm further imposes a unity gain constraint at each Doppler frequency such that,

$$\underline{S}^t(f) \underline{W}_0 = 1 \quad (16)$$

Applying this constraint to (11) and substituting back into (15) results in,

$$P_m(f) = \left[\frac{1}{\underline{S}^t(f) \cdot \hat{\underline{R}}_m^{-1} \cdot \underline{S}^*(f)} \right] \quad (17)$$

Therefore, upon sweeping the deterministic "steering" vector, $\underline{S}(f)$, through the Doppler frequency range of interest, the estimated power spectrum will be plotted for the m^{th} rangebin. In addition to estimating the spectral lines, the MLM algorithm provides other useful performance characteristics:

- a) It evaluates the relative power levels of estimated spectral lines because of the gain constraint in equation (16).
- b) It is one of the few adaptive algorithms that permits "copy" of a desired narrow spectral band [8], i.e., it will pass the desired narrow band while rejecting all other frequency components in an optimal manner. This feature will be used extensively in section 4.

It's computation burden is similar to that of the SMI algorithm, i.e., it requires data storage in the sample covariance matrix and must compute the inverse.

"Beamspace" LPF Algorithm

This technique is patterned after a spatial beamspace method described by Gabriel [19], and is intended to permit focussing upon a small sector of the overall image. It achieves wide-aperture high-resolution, but yet requires

only a relatively small number of degrees of freedom (DOF) in the processing. Fig. 3 illustrates the technique applied to a time-domain Doppler processor, wherein a 64-tap delay line receives the input data samples. Thus, dimension $N=64$ in the \underline{D} matrix described above. System DOF are reduced in two steps: first a multiple sub-band DFT connects into the even-numbered taps only (a 32-point DFT); and second, we select only 15 of the output sub-bands to cover our Doppler sector of interest. The resultant output Doppler filter passbands are shown plotted in Fig. 4. Fig. 3 also shows a shaped reference filter connected into seventeen (17) adjacent taps, numbers 48 through 64. The tap weighting is chosen to pass only the frequencies within the Doppler sector of interest, and to reject all others. Fig. 5 illustrates the response of our example reference filter. Thus, we end up with just sixteen filter outputs to process, instead of 64, and can proceed with almost any of the current high-resolution algorithms, including the algorithms described above.

3. Simulated Data Results

Rotating Boom Model: Simulated data samples are generated from several different point-target models. Fig. 6 illustrates the first of these, based upon a rotating-boom along which are located fifteen (15) targets. The angle of the boom with respect to the direction of the radar is defined as $\theta(t)$,

$$\theta(t) = 2\pi \left[\frac{1}{4} + \left(\frac{f_r}{60} \right) t \right] \quad (18)$$

where f_r is the rotation rate of the boom in revolutions per minute (rpm), and t is the time variable in seconds. The range of the i th target, $X_i(t)$, from a zero-range reference point may be written,

$$X_i(t) = D_c - d_i \cos(\theta(t)) \quad (19)$$

where d_i is the distance from the center of the boom to the i^{th} target, and D_c is the distance from the zero-range reference point to the center of the boom. Range-rate velocity, $V_i(t)$, of the i^{th} target is given by the first derivative of $X_i(t)$,

$$V_i(t) = \frac{dX_i(t)}{dt} = -2\pi \left(\frac{f_r}{60} \right) d_i \sin(\theta(t)), \quad (20)$$

and we can then readily compute the Doppler frequency, $f_i(t)$, via the RF wavelength, λ ,

$$f_i(t) = \left(\frac{2}{\lambda} \right) V_i(t) \quad (21)$$

The factor of 2 in (21) occurs because of the two-way path of radar RF energy [13]. Table 1 contains the parameter values associated with the 15 point-targets located along the boom, together with their Doppler frequencies computed from (21). Five targets were given a signal-to-noise ratio (SNR) of 23 dB, two of 20 dB, one of 10 dB, and the remainder 0 dB. Some targets were grouped together to deliberately produce closely-spaced Doppler signals that would require superresolution to separate. Data samples were accumulated from 200 prf (total) as the boom swung through broadside.

Complex data samples as utilized in (1) may be computed for any given sample time, t , that is synchronized with the radar prf and our selected range window,

$$E_m(t) = \sum_{l=1}^{L_m} A_l(t) + \eta_m(t) \quad (22)$$

$$t = t_0 + \left(\frac{k}{\text{prf}} \right) \quad (23)$$

where m is the rangebin index

L_m is the number of targets within the m^{th} rangebin

$\eta_m(t)$ is the receiver noise sample for the m^{th} rangebin

k is the time sampling index

t_0 is a start-time parameter

The $A_l(t)$ are determined from a rangebin test conducted for all pertinent targets at time t ,

$$\left| r_m - X_i(t) \right| \leq \left(\frac{\Delta}{2} \right) \quad (24)$$

where Δ is the rangebin dimension

r_m is the m^{th} rangebin distance

and $X_i(t)$ is defined in (19). Note that the index l will be associated with our target index i as determined from (24), and that we simply substitute those particular targets (if any) into (22) as

$$A_l(t) = A_i e^{j\psi_i(t)} \quad (25)$$

$$\psi_i(t) = -4\pi \left(\frac{X_i(t)}{\lambda} \right) \quad (26)$$

where the amplitudes, A_i , correspond to the SNR's given in Table 1. The reader will note that the target phases in (26) depend upon the range in wavelengths at each prf sampling time t .

Fig. 7 shows the Doppler spectrum estimates for nine of the targets along the boom, computed from the data taken in the particular rangebin occupied by the boom in its broadside position, i.e., this is a Doppler spectrum for a single rangebin cut. Utilizing the processor arrangement illustrated in Fig. 3, our delay line gives us an overall Doppler gradient window-aperture of $N=64$ taps, which implies a sub-band filter conventional resolution of $360/64 = 5.63$ degrees in the z -plane (prf-normalized Doppler radians converted to degrees). Fig. 4 verifies this sub-band filter resolution. Therefore, note in fig. 7 that we have a target doublet and a target triplet in which the Doppler frequencies are separated by less than 3 degrees, or about half of conventional resolution capability. Fig. 7(a) demonstrates that the conventional Fourier transform is not able to resolve the nine individual point-targets that occur within the plot region. Yet those targets have been resolved by both of the spectral estimation algorithms utilized, clearly demonstrating superresolution for this example. In Fig. 7(c) we note that the MLM algorithm not only resolves the targets, but also gives the correct relative power level. Finally, on the right-hand side of the Fig. 7 plots, there are four Doppler signals of significantly different power levels and spaced one beamwidth apart. This type of situation defies resolution by conventional filters of 64 taps because of their beamwidths and/or sidelobes, and yet the two superresolution algorithms have readily resolved the four signals. A conventional FFT processor would require an aperture several times larger than our 64 taps in order to resolve these nine individual point-

targets, and, therefore, may actually require more prf data samples to achieve the same resolution. Note in this example that $N=64$, $K=140$ updates per (8), and there was a total of 200 prf data samples available.

A point of clarification is in order concerning the appropriate measure of resolution for comparison. It is well known that temporal frequency resolution varies inversely with the processing time duration [5]. For the example given in TABLE 1, we have a prf of 418 and 200 samples processed, resulting in a processing time duration of 0.48 seconds or a temporal frequency resolution of 2.1 Hz. However, this ultimate resolution assumes uniform weighting of the data samples plus the utilization of all 200 samples to get a single output pulse in adjacent filter bins - assumptions that are often not applicable in practical systems. Doppler filters often have tapered weighting to reduce sidelobes and, in addition, utilize some form of output pulse integration. Thus, a reasonable measure for resolution comparison should be based upon the particular system under consideration.

Targets Entering/Leaving a Rangebin: Before we begin to demonstrate three-dimensional (3D) imaging of rotating objects, it is necessary to address the deleterious effects associated with targets that are either entering or leaving a rangebin. Whenever the returns from a target fail to fill our tapped delay line in a given rangebin, then we no longer have a complete gradient aperture and the target energy will not focus into a narrow Doppler band. Instead, the energy tends to spread out in accordance with its partial aperture, resulting in a smeared/faulty Doppler spectrum estimate.

One technique for diminishing such faulty spectrum effects is to monitor the tap power in both halves of the delay line and form two sums that would be sensitive to a strong target entry-exit,

$$S_{ml}(k) = \sum_{n=1}^L |E_{mn}(k)|^2, \quad \text{left half sum}, \quad (27)$$

$$S_{mr}(k) = \sum_{n=L}^N |E_{mn}(k)|^2, \quad \text{right half sum} \quad (28)$$

where $L = \left(\frac{N}{2}\right)$ and $E_{mn}(k)$ is defined in (1).

These sums must usually be augmented with a bias term to prevent excessive noise triggering.

$$S_1 = S_{ml}(k) + \left(\frac{L}{2}\right) \sigma_o^2 \quad (29)$$

$$S_2 = S_{mr}(k) + \left(\frac{L}{2}\right) \sigma_o^2 \quad (30)$$

where σ_o^2 is the average noise power level per tap. We then form a power-sensitive threshold level, Q , which may be of the form,

$$Q = 1.8 \left[1 + \frac{2N\sigma_o^2}{S_1 + S_2} \right] \quad (31)$$

If the ratio of $\left(\frac{S_1}{S_2}\right)$, or its reciprocal, exceeds the value of Q , then that particular rangebin signal vector is skipped, i.e., it is not utilized in the algorithm update processing.

A better technique that is applicable to targets of low SNR is to apply an FFT to both halves of the delay line, such that we now divide the rangebin signal vector energy into L Doppler filter bins as indicated in (2) through (5). Note that each filter bin has a power gain equal to L , thus enhancing targets of low SNR. If a target is entering a rangebin, its Doppler energy will be strong in its right-half Doppler bin, but non-existent in the same

Doppler bin on the left-hand side; and vice-versa if a target is leaving a rangebin. Therefore, the ratio of the power in each Doppler bin must be compared for the two halves in a manner very similar to (29) through (31), and particular rangebin signal vectors are skipped if the threshold is exceeded. The performance of this FFT technique is much superior to the simpler technique described in (27) through (31), but it also requires considerably more computation in doing the FFT's and then testing each Doppler filter bin.

Merry-go-round Model: The second simulation model is based upon a "merry-go-round" of 24 point-targets, as illustrated in Fig. 8. The targets are equally spaced on a circle of 35 meters radius and the entire assembly is rotated at a rate of 0.63 rpm. Target reflection coefficients are chosen such that the odd numbers have a receiver output signal-to-noise ratio, (SNR) of 5 dB, and the even numbers have an SNR of 25 dB. Thus, they alternate in strength around the circle. In addition, a stationary target of 25 dB SNR is placed at the center of the circle to serve as a zero-Doppler reference.

From Fig. 8, we can compute the angle position of the i^{th} target, $\theta_i(t)$, at time t

$$\theta_i(t) = 2\pi \left[\left(\frac{i-1}{I} \right) + \left(\frac{f_r}{60} \right) t \right] \quad (32)$$

where I is the total number of equi-spaced targets and f_r is the rotation rate in rpm. The range of the i^{th} target, $X_i(t)$, from a zero range reference point may be written,

$$X_i(t) = D_c - d_o \cos(\theta_i(t)) \quad (33)$$

where D_0 is the distance from zero-range reference point to the center of the circle, and d_0 is the radius of the circle. Range-rate velocity, $V_i(t)$, and Doppler frequency, $f_i(t)$, then follow as in (20) and (21). Complex data samples may be generated from this model in the same manner as described for the rotating boom model.

Fig. 9 shows a typical three-dimensional range-Doppler radar image for this particular rotating object. The upper portion of Fig. 9 illustrates the "image truth", i.e., it plots the point-target SNR's at their exact range-Doppler coordinate locations on the "merry-go-round". The lower portion of Fig. 9 illustrates a 3D image estimate of the rotating object, utilizing the simple H-A algorithm described in the previous section. Parameter values include $M=90$ rangebins, $N=32$ delay line taps, and $K = 140$ prf processed. Comparing the estimate against the "image-truth", we note that the H-A algorithm has correctly located all 24 point-targets around the circle. On the negative side, this simple algorithm does not give us the relative power levels of the target, and, in addition, it has a rather "noisy floor" that will require thresholding to enhance the image.

Fig. 10 illustrates a second 3D image estimate of this rotating object, utilizing the more desirable MLM algorithm described in the previous section. Recall that the MLM algorithm has a much greater computation burden than the H-A algorithm but, in return it also estimates the relative power levels of the targets in addition to their locations. Fig. 10(a) was processed without any regard for target entry/exit effects, and it contains several examples of the smeared/faulty Doppler spectrum problems referred to above. In contrast, Fig. 10(b) was processed utilizing the FrT entry/exit routine, and it will be noted that all of the problem target spectra were

eliminated. Another technique utilized in Fig. 10 to enhance the image was the use of a 2 dB output threshold level, which tends to diminish the "noisy floor" effect (compare against Fig. 9(b)).

4. Range Domain Superresolution

The problem of resolving an unknown number of closely spaced, overlapping, and noisy echoes of a signal with apriori known shape is common to several application areas such as radar, sonar, geological acoustic sounding, ultrasound-based nondestructive testing, and medical imaging procedures. Several approaches for solving this problem have been described in the literature. These include detection/deconvolution schemes, inverse filtering, least squares, and maximum likelihood methods [20-25]. In the radar area, we are familiar with various pulse compression schemes [13] that have been applied to this problem. Recently, Bruckstein et al [26] have described a new method for achieving high resolution in such cases, based upon an eigenstructure technique which exploits the structure of the received signal covariance matrix. This new method was instrumental in prompting the current investigation. Also, high resolution techniques have been applied to the wideband linear FM ranging method [5,27,28].

Consider the familiar rectangular pulse with linear FM chirp shown in Fig. 11. This type of pulse [13] is utilized as an example of a radar signal of known shape, $S(t)$, throughout the remainder of our discussion. $S(t)$ may be expressed mathematically in the form,

$$S(t) = \frac{1}{\sqrt{T}} \text{rect}\left(\frac{t}{T}\right) \exp\left(\frac{j\pi B t^2}{T}\right), \quad -\frac{T}{2} < t < \frac{T}{2}, \quad (34)$$

where T is the pulse duration (width), B is the modulation bandwidth, and t is the time variable. The exponent term gives us the phase modulation during the pulse, $\Psi(t)$,

$$\Psi(t) = \frac{\pi B t^2}{T}, \quad -\frac{T}{2} < t < \frac{T}{2} \quad (35)$$

and the first derivative of $\Psi(t)$ gives the frequency modulation (chirp)

$$F(t) = \frac{1}{2\pi} \frac{d\Psi(t)}{dt} = \left(\frac{Bt}{T}\right), \quad -\frac{T}{2} < t < \frac{T}{2} \quad (36)$$

Characteristics of interest include the time-bandwidth product, BT , the approximate time resolution given by the reciprocal, $\frac{1}{B}$, and the pulse compression ratio, D ,

$$D = \left(\frac{T}{\frac{1}{B}}\right) = BT \quad (37)$$

We are also interested in delayed and scaled versions of our known waveform that would correspond to the range locations of scattering objects/point targets,

$$\alpha_i S(t - T_i), \quad (T_i - \frac{T}{2}) < t < (T_i + \frac{T}{2}) \quad (38)$$

where $T_i = \left(\frac{2r_i}{c}\right)$, the round-trip time delay associated with the i^{th} point-target at range r_i , c is the velocity of light, and α_i is the scattering coefficient.

The assumptions discussed in the beginning paragraph of Section 2 also apply here, except for one important, fundamental difference. For our range domain processing, the sampling must be performed prior to the pulse compression filter. The reason for this requirement is that the pulse compression filter will be utilizing adaptive weighting, rather than conventional deterministic matched filter weighting. One of the implications of this fundamental difference is that we must first define an uncompressed, digital-data signal vector, \underline{U}_k , within our range window,

$$\left[\underline{U}_k^t = U_k(t_1), U_k(t_2), U_k(t_3), \dots, U_k(t_Q) \right] \quad (39)$$

where the subscript k denotes the k^{th} prf period, and subscripts 1 through Q denote the q^{th} data sample. This uncompressed signal vector may be processed via various pulse compression algorithms to obtain desired range-domain response. Brief descriptions of a few such algorithms follow.

Matched Filter DFT

First, let us compute the conventional matched filter pulse compression response wherein we require matched filter weights, $W(t)$ at time $t = T$ corresponding to a given range. Briefly, we desire the complex conjugate of (34), but including a linear phase term to account for the time delay phase shift,

$$W(t-T) = \frac{1}{\sqrt{T}} \text{rect}\left(\frac{t-T}{T}\right) \exp(-j\Psi(t-T)) \quad (40)$$

$$\text{and } \Psi(t-T) = \left(\frac{\pi B}{T}\right)(t-T)^2 - \omega_0 T \quad (41)$$

$$\text{subject to } \left(T - \frac{T}{2}\right) < t < \left(T + \frac{T}{2}\right)$$

where $\omega_0 T$ is the linear phase term to account for the time delay phase shift. In practice, there is a total linear phase term of $\omega_0(t-T)$, but we delete the reference RF carrier phase, $\omega_0 t$, for the sake of simplicity in the expressions. Since we are dealing with a precise sampled-data system, (40) and (41) must be written in terms of integer multiples of the sampling time, Δt , which is hereafter assumed to be normalized to unity, i.e., $\Delta t = \frac{1}{B} = 1$. This implies that our bandwidth, B , is also normalized to unity. Further, we may account for the carrier time delay phasing via the number of RF wavelengths per Δt interval.

Note that our signal vector \underline{U}_k in (39) corresponds to this model, and we have these precise sampling times denoted as t_q , where the range window extends from $1 \leq q \leq Q$. The waveform of Fig. 11 has a width smaller than Q and, from (37) we find that the number of samplings, N , within the waveform is equal to the pulse compression ratio, i.e., define $N = \text{INT}(D)$ where $\text{INT}(\quad)$ means the integer value of the argument. Applying the waveform time restriction, it follows that the values of t_q within the waveform for delay T must be,

$$(T - \frac{T}{2}) < t_q < (T + \frac{T}{2}) \quad (42)$$

$$\text{or} \quad -\frac{T}{2} < (t_q - T) < \frac{T}{2}$$

If T is expressed in terms of sampling units, then we may define an integer index l , such that

$$l = \text{INT}(T + .5) \quad (43)$$

and this integer serves as an index for individual rangebins within the overall range window. Also, it permits us to define an index n that applies only within the waveform,

$$\text{define } t_n = \frac{1}{2}(2n-N-1) + \ell \quad \text{for } N \text{ odd,} \quad (44)$$

$$\text{such that } -\frac{T}{2} < (t_n - T) < \frac{T}{2}. \quad (45)$$

$$\text{Therefore } (t_n - T) = \frac{1}{2} (2n-N-1) - (T-\ell) \quad (46)$$

$$\text{where } 1 \leq n \leq N$$

From (42) it is evident that the t_n may be associated with N values of t_q via a simple index shift,

$$q = n + \ell \quad (47)$$

Substituting (46) into (40) and (41) gives us our matched filter weights, $W_n(t-T)$, and we can apply them to the signal vector \underline{U}_k to obtain a conventional DFT compressed pulse output,

$$V_k(T) = \sum_{n=1}^N U_k(t_q) W_n\left(\frac{1}{2}(2n-N-1) - (T-\ell)\right) \quad (48)$$

where index q is given by (47) above. The variable, T, becomes our parameter for "sweeping" or "stepping" across the range window. Recall that $T = (\frac{2r}{c})$.

Equation (48) illustrates mathematically how the waveform operates upon the signal vector \underline{U}_k to generate a DFT compressed pulse output for a target located within a particular rangebin. Note that the variable, $(T-\ell)$, functions as a vernier shift for each of the N sampling times within the waveform.

MLM Algorithm

The description of this algorithm in Section 2 applies equally to the range domain, and it is an important algorithm because it allows us the "copy" privilege. That is, it can pass the signal in a narrow band around the target range of interest, and minimize or reject all other target signals in an optimal manner.

To utilize the algorithm, we must form the familiar sample covariance matrix, $\hat{\underline{R}}$, in the range domain. $\hat{\underline{R}}$ may be averaged over K updates in a manner similar to equation (8) in the Doppler domain,

$$\hat{\underline{R}} = \frac{1}{K} \sum_{k=1}^K \underline{U}_k^* \cdot \underline{U}_k^t \quad (49)$$

However, an important difference is that we do not require filling all elements within the matrix dimensions of $Q \times Q$, since the compression filter weights only have a dimension equal to N . Thus, the indices of our matrix elements, R_{mn} , in the stored upper triangle (12) may be limited to $(n-m+1) \leq N$ where m is the row index, and n is the column index.

Because the dimension N is considerably smaller than Q , it is advantageous to extract from $\hat{\underline{R}}$ a series of smaller matrices denoted as $\hat{\underline{R}}_i$, where their dimensions are exactly $N \times N$ and the subscript, i , is related to the row/column subscripts as follows,

$$\begin{aligned} (i+1) \leq m \leq (i+N) \\ (i+1) \leq n \leq (i+N) \end{aligned} \quad \begin{aligned} i=0,1,2,3,\dots,(Q-N) \end{aligned} \quad (50)$$

This results in a total of $(Q-N+1)$ smaller matrices which are to be inverted and stored for use in processing.

To compute the MLM optimum adaptive weights for "copy" purposes, we first substitute (40) into (11) to get the Weiner weights,

$$\underline{W}_0(t-T) = \mu \hat{R}_i^{-1} \underline{W}(t-T) \quad -\frac{1}{2} < (t-T) < \frac{T}{2} \quad (51)$$

where index $i = \ell$ per equation (43).

It should be noted that we are using the conventional matched filter vector as our "steering" vector. The scalar μ is next evaluated as the MLM power output per (17), and substituted back into (51) to give us gain-normalized MLM optimum "copy" weights. The reader should recognize that (51) results in adaptive pulse compression filter weights which tend to null out any target returns that are not at the range represented by T .

A subtle requirement embodied within (51) is the small matrix index, i . As we "sweep" or "step" our steering vector via the value of T , then the correct i^{th} matrix inverse must be utilized. This index value follows from (43) and (47). Each rangebin requires its associated small matrix, i.e., if we are sweeping across a range window consisting of 30 rangebins, then we need 30 small matrices. A given small matrix permits optimum weights to be computed anywhere within the extent of its associated rangebin, i.e., within $\pm 1/2$.

The MLM adaptive "copy" weights are utilized in exactly the same manner as conventional matched filter weights in (48). However, the vernier shift permitted by $(T-\ell)$ is now of considerable interest because of our intention to achieve range resolution finer than a single sampling period (or rangebin).

SLC Algorithm

This algorithm is derived from its well-known counterpart in the spatial domain, the "sidelobe canceller" (SLC) [14, 17] which, in turn, is intimately linked to the familiar linear prediction filter of spectral analysis [6]. The algorithm is widely used because it is relatively simple to implement in most applications, and yet exhibits excellent adaptive filter performance characteristics. The unique feature of this algorithm is its simple "steering" weight vector, which consists of zeros except for one element. For example, in (51) our "steering" vector becomes,

$$\underline{w}^t(t-T) = [1, 0, 0, \dots, 0.0,] \quad (52)$$

and it is evident that the optimum Weiner weight will then consist of the first column of the inverse of the small sample covariance matrix. To identify its special nature, the resulting optimum weight is referred to as the Weiner SLC adaptive weight, and it is standard practice to compute a value for μ such that the first element of this SLC weight is always normalized to unity.

A particularly attractive version of the SLC algorithm results when it is based upon the H-A algorithm discussed in Section 2, because then the computation burden is minimal. As explained therein, sample covariance matrices are not required, since updates are integrated directly into the adaptive weights themselves.

Coherent Target Scatterers

When target objects contain scatterers that have no relative motion when viewed from the direction of the radar, then we have a special situation

defined as "coherent scatterers." This phenomenon has an equivalence in the spatial domain and has been addressed in the literature by a number of authors [6,11,29]. It can result in severely degraded resolution performance from superresolution algorithms, and usually requires additional processing techniques to overcome.

To begin with, the reader is reminded that the sample target data from a single radar waveform transmission (prf) is inherently coherent, in a manner analogous to taking a single data "snapshot" across a spacial domain array of elements. For this singular situation the FFT matched filter (beamformer) is perfectly operable at full aperture resolution, whereas superresolution techniques are not. This is one of the reasons why superresolution techniques must be considered as complementary/junior to the FFT. Superresolution techniques do not become competitive until after a reasonable number of prf data samplings are available for processing.

The crucial requirement is to have enough samplings (observation time) to permit decorrelation of multiple point-targets within a rangebin (analogous to multiple sources within a beamwidth in the spatial domain). In essence, we seek stationarity of the scatterer phase data, as if they were sources of random phase signals. There are several ways in which the necessary decorrelation might be achieved, or at least approximated:

- a. A slowly rotating object wherein the scatterers have sufficient doppler differences. This is a classic ISAR situation [1-5].
- b. An object in straight-line motion (non-radial) wherein an equivalent rotation occurs over the observation time [5,12].
- c. A stepped linear FM carrier shift (small increment per prf) which produces sufficient phase changes between scatterers spaced closely in

range. This borrows from the classic linear FM ranging method [5,13].

d. Random frequency hopping of the carrier per prf to produce sufficient phase changes for small range separations.

e. Combinations of the above.

It is sometimes helpful to view the above decorrelation methods in terms of the variance of the first derivative of the ratio $(\frac{x}{\lambda})$, where x is the range separation between two closely-spaced scatterers.

$$\text{Variance of } \frac{d(x/\lambda)}{dt} \geq 1 \quad (53)$$

$$\text{Doppler Difference} = \left(-\frac{1}{\lambda}\right) \frac{dX}{dt} \text{ Hz} \quad (54)$$

$$\text{Carrier Shift} = x \frac{d(1/\lambda)}{dt} \text{ Hz} \quad (55)$$

There are a number of situation conditions and subtle limitations involved in the above methods, which are not addressed in this initial report because of space considerations. Further research investigations are needed to clarify some of these. The simulation examples contained in this report are based primarily upon method (a), the slowly rotating object.

Simulated Data Results

Simulated data samples have been generated from a rotating-boom model similar to Fig. 6, along which are located three targets. TABLE 2 contains the parameter values, together with their Doppler frequencies computed from (21). The parameter values were deliberately chosen to produce close target spacings that would require superresolution in both the range domain and the Doppler domain. The pulse compression ratio of our chirp waveform is D=13.

Uncompressed digital data samples are entered into our signal vector, \underline{u}_k , per (39), and are utilized in accumulating a sample covariance matrix over $K=264$ prf updates per (49). Fig. 12a illustrates typical conventional DFT matched filter responses plotted during this accumulation time, and represents examples of the $V_k(T)$ output sequences per (48). The reason for the large spread in the power plot values is the continuously changing phase relationships between the three targets due to the different Dopplers. Fig. 12b shows the averaged matched filter response (7) over all K prf updates. Fig. 12 clearly demonstrates that our three targets are too close together to be resolved by conventional pulse compression. The somewhat "jerky" behavior in the range "sidelobes" is due to the waveform entry/exit effects as it sweeps across.

After $\hat{\underline{R}}$ is accumulated, we extract the series of smaller matrices, $\hat{\underline{R}}_i$ per (50) and compute their inverses for use in (51). Figure 13 then illustrates the target estimate plots obtained from the MLM algorithm (17), and the Weiner SLC algorithm weight per (51) & (52). Note that both of these superresolution algorithms clearly resolve the three targets and accurately locate their range positions. In addition, the MLM algorithm correctly estimates the relative power levels of the targets.

The next step is to take advantage of the "copy" feature referred to in the description of the MLM algorithm. This feature is so important to our processing that it is re-iterated here again; i.e., the MLM optimum "copy" weights in (51) permit us to pass the signal in a narrow region around the target range of interest, and minimize or reject all other target signals in an optimal manner. This feature allows us to obtain adaptive compressed-pulse output signals at vernier steps in range. For the current simulation example

described in TABLE 2, each sampling period (or rangebin) is divided into ten subdivisions, and an output data sample is computed for each subdivision via (51) and (48). Fig. 14 shows four typical "copy" weight responses in the range domain for various "steering" range selections. Starting at the upper left, the range mainlobe is steered to range 12.0 whereby the three targets are all located in the sidelobe region and readily nulled out. In the upper right figure, the range mainlobe is steered to range 14.0 whereby the target located at 14.3 is encroaching into the mainlobe and results in high adaptive sidelobes (compare with upper left pattern). However, note that all three targets are still nulled out. The two lower figures illustrate the mainlobe steered directly into target locations at ranges 14.3 and 15.0. Note that the unity gain constraint (16) results in passing the target signal at the steered range, while simultaneously nulling out the other two, i.e., a clear demonstration of the "copy" feature. Fig. 15 illustrates the results obtained from applying this feature to the rangebin region extending from range 12.0 to 18.0. Compare against Fig. 12. Since we are increasing the number of output data samples by a factor of ten, it becomes expedient to apply this technique over a smaller field of view. Thus, our range field is restricted to six rangebins in this case, from range 12.0 to 18.0, but that generates 60 vernier data samples per prf. The 60 data samples per prf are then processed in the Doppler domain in exactly the same manner as described in Section 2.

5. Combined Range/Doppler 3D Superresolution Imaging

Three different processing techniques are utilized to demonstrate combined Range/Doppler 3D superresolution radar imaging:

- a. Conventional Fourier Transform
- b. MLM/LPF Algorithm
- c. Digital image from optimum weight roots.

Simulated radar data samples were generated from the rotating-boom model described in Section 4 above, wherein we have three point-targets of 10dB SNR located along the boom. TABLE 2 contains the various parameter values which were deliberately chosen to produce close target spacings of 0.7 units in both the range and the Doppler domain, i.e., the targets are separated by only 0.7 of a conventional rangebin in the range domain, and 0.7 of a conventional "Doppler bin" in the Doppler domain. Note the slow boom rotation rate of only 0.1 rpm.

Conventional Fourier Transform

Figure 16(c) shows the conventional Fourier transform image processed from the simulated radar data samples. The Fourier transform serves as a baseline reference to illustrate what conventional processing would result in. Uniform illumination matched-filter weighting was utilized in both domains, resulting in maximum conventional target resolution but with the associated high sidelobes. An image threshold level of 15 dB below peak power level was imposed in order to eliminate the distracting effects of the high sidelobes, and it will be noted that only the first sidelobes (13 dB down) are visible in the image. At maximum conventional resolution, we note that the 3D image just barely manages to resolve the three point-targets because their separation along the range/doppler diagonal is unity, i.e., the square-root of the sum of the squares of their 0.7 spacings. Recall from Fig. 12b that resolution in only the range domain was not possible. Furthermore, if we were to utilize a tapered matched-filter weighting in order to reduce sidelobe levels, then the

3D image would no longer resolve the targets because of the increase in the "beamwidths".

MLM/LPF Algorithm

Fig. 16(b) shows the image obtained when the same simulated radar samples are processed via the MLM/LPF Algorithm. Recall that this algorithm was described in Section 2 for the Doppler domain (see Fig. 7c), and in Section 4 for the range domain (see Fig. 13b). The "copy" feature of the MLM algorithm was utilized for each vernier range subdivision within the small field of view represented by the rangebin scale in Fig. 16, i.e., 90 vernier data samples per prf. The MLM algorithm has such well-behaved filter residue characteristics (an adaptive equivalent of "sidelobes") that the image threshold level can be set just slightly above the receiver noise level, about 2 dB for Fig. 16(b), thus eliminating the "noise floor" from the image. Note that the three targets are clearly resolved in this image, their locations are correct, and their relative power levels are accurately represented. It is obvious that the three point-targets could be located much closer together and still be resolved. Although the MLM algorithm worked well in this particular example, it has a few drawbacks that must be considered:

- a. The computation/processing burden is high.
- b. It has the poorest resolution capability of all superresolution techniques.
- c. There is a wide spectral spread in the Doppler energy for vernier range subdivisions close to a target location. This

Doppler energy spread is caused by the high sidelobes of the "copy" weights when our mainlobe is steered close to target locations, i.e., the high sidelobes amplify the power level of noise and signal residue across the Doppler band. It produces a "corrugation effect" in the images, which is evident in Fig. 16.

Digital Image from Optimum Weight Roots

There are several different methods available for addressing the drawbacks of the MLM algorithm, and the one chosen for our next image display is described as a "digital" 3D plot technique based upon optimum weight roots. Fig. 16(a) illustrates the 3D image formed when the same simulated radar data samples are processed via this technique. Note that the image now exhibits excellent fidelity with the model truth, and there are no distracting artifacts except for some minor "noise floor" pips.

The processing begins in the range domain by accumulating the sample covariance matrix and extracting the series of smaller matrices denoted as \hat{R}_i as described in Section 4. It is only necessary to extract the nine smaller matrices associated with the rangebins to be displayed. These nine matrices are inverted, stored, and utilized to compute the nine optimum weight vectors needed, i.e., we compute one adaptive filter weight vector per rangebin. Fig. 13a is a "range spectral estimate" obtained from those weight vectors, with the nine rangebins extending from range 10.5 to 19.5 as plotted there. The sharp peaks correspond to roots of the adaptive filter weights which represent the target range locations, so we solve for those range locations by utilizing a peakfinder routine.

The peakfinder routine readily detects the three target locations within its field of view extending from range 10.5 to 19.5. For our current simulation example, those three locations were estimated as 14.3, 15.0, and

15.7. Knowing those locations gives us the opportunity for dramatic reductions in computer processing burden, because we now require the "copy" feature of the MLM algorithm only at the three estimated target locations, instead of the 90 vernier range divisions that would otherwise be computed to cover the entire field of view.

Next, the "copy" vernier data samples for the target locations are processed in the Doppler domain via the "Beamspace" LPF algorithm of Section 2, from which we compute associated adaptive weight vectors for the tapped delay line. The roots of these weight vectors in the Doppler domain give us an estimate of the Doppler frequencies. A standard polynomial root finding routine is utilized for this purpose. Knowing the frequencies, the MLM algorithm is then applied to get the relative power levels and thus estimate the power of the spectrum. Once again, we have a dramatic reduction in computer processing burden through having an estimate of the particular Doppler frequencies.

The final step consists of plotting the estimated power spectral lines at their estimated target range locations, resulting in the "digital" 3D image of Fig. 16(a). This method overcomes all three of the drawbacks noted for the MLM/LPF Algorithm images, and opens up the possibility for practical technology development.

Triangle Model of Ten Point-Targets

To demonstrate performance against a more complicated rotating object, the final simulations consist of ten point-targets arranged in the shape of a triangle as shown in Fig. 17. TABLE 3 contains the various parameter values which were deliberately chosen to result in close target spacings and to fill three adjacent rangebins with combinations of three or four targets each.

Also, note that five of the targets have an SNR of 0 dB. Data samples from 264 prf (total) were processed.

Range estimate plots are given in Fig. 18 for four different algorithms: Fourier, MLM, Wiener SLC, and MUSIC [30]. It is of interest to note the progression of resolution. DFT processing gives us the overall "power envelope" of the ten targets in range; MLM processing separates them into three crude groups; Wiener SLC refines the estimate further by indicating that at least four targets are present; and MUSIC has sufficient sensitivity to indicate that at least five targets are present, plus a number of extraneous artifacts. The latter algorithm is a sensitive high-resolution technique based upon the noise eigenvectors of the covariance matrix. References [26,30] are recommended for those readers who are interested in further details on the MUSIC algorithm.

Fig. 19 then illustrates the two-dimensional radar images processed via the same three algorithms as used for Fig. 16. The conventional Fourier transform plotted in Fig. 19(c) again serves as a baseline reference to illustrate the results of conventional processing. Here we can barely discern a crude triangular shape within which at least six components are evident. The MLM algorithm plotted in Fig. 19(b) successfully resolves all ten targets, although accompanied by some smearing, location displacements, and the "corrugation" effect referred to earlier. Recognition of the overall triangular shape and component scatterers is accomplished. The digital image plotted in Fig. 19(a) then refines the estimate and enhances the component scatterers. Note that the digital image does contain a few extraneous artifacts, but these are not considered to be serious defects because such artifacts tend to move around (or scintillate) as successive images are processed, whereas the true scatterers remain stable.

Triangle Model with Coherence Present

In section 4 we alluded to the deleterious phenomenon defined as "coherent scatterers" wherein two or more closely-spaced scatterers have the same Doppler frequency as seen by the radar. Our final simulation example is deliberately designed to illustrate such a case. TABLE 4 contains the various parameter values for the ten targets, and it will be noted that coherence exists (same Doppler) between targets No. 2 and No. 10, No. 4 and No. 9, and No. 6 and No. 8. Thus, three pairs of scatterers within the triangle are coherent.

Fig. 20 illustrates the radar image results, utilizing the same three algorithms as before. The conventional Fourier transform plotted in Fig. 20(c) gives us a crude triangular shape in which it is difficult to pick out any component parts beyond the corners of the triangle. The MLM algorithm plotted in Fig. 20(b) does a little better in resolving component parts, but note that it also generates some distracting outboard artifacts from the processing. The digital image plotted in Fig. 20(a) then refines the estimate and enhances the component scatterers, but still includes the rather strong outboard artifacts. Careful study of several coherence cases has revealed the following deleterious effects:

- a) the positions of such scatterers may be shifted in both range and/or Doppler.
- b) such scatterers may blend to appear as a single scatterer at intermediate positions.
- c) the processed power levels may not be correct.
- d) strong artifacts may be generated at range/doppler positions where no scatterer exists.

Fig. 20 contains all of the above effects, and the net result is distortion of the processed image. To overcome these effects, it is necessary to employ a decorrelation method such as the carrier shift techniques discussed in Section 4.

6. Conclusions

High-resolution optimal estimation techniques have been applied to the problem area of radar imaging of rotating objects. Typical digital range-Doppler processor operations are described, utilizing several of the many spectral analysis estimation techniques available in the literature. Their application to the range domain represents new R&D work, wherein multiple scatterers within one rangebin have been resolved without increasing the bandwidth. Quality ISAR images have been obtained from simulated radar data generated from point-target models of rotating objects. These simulation results demonstrate the feasibility for achieving superresolution in the Doppler domain, the range domain, and both domains jointly. The capability for focusing upon a small section of the overall image and achieving finer detail (magnification) is particularly useful. It is concluded that superresolution techniques offer a viable complement to conventional DFT-ISAR image processing, and should permit either higher resolution images from the same data samples, or equal-quality images from significantly fewer data samples.

Further research is needed in several areas including algorithm development, algorithm comparison, meaningful resolution comparison criteria, pulse-compression waveform design/comparison, adaptive "focussing" upon dominant scatterers, techniques for reducing computer burden, the relationship between image quality and number of data samples, the special problem area of

coherent target scatterers, rangebin entering/leaving effects, and the evaluation of these techniques when processing experimental radar data samples.

REFERENCES

1. D.A. Ausherman et al, "Developments in Radar Imaging," IEEE Trans. Aerospace and Elect. Sys., Vol. AES-20, No. 4, pp. 363-400, July 1984.
2. J.L. Walker, "Range-Doppler Imaging of Rotating Objects," IEEE Trans. Aerospace and Elect. Sys., Vol. AES-16, No. 1, pp 23-52, Jan. 1980
3. C. C. Chen and H. C. Andrews, "Target-Motion-Induced-Radar Imaging," IEEE Trans. Aerospace and Elec. Sys., Vol. AES-16, No. 1, pp. 2-14, Jan 1980.
4. M. J. Prickett and C. C. Chen, "Principles of Inverse Synthetic Aperture Radar (ISAR) Imaging," IEEE 1980 EASCON Record, p. 340.
5. D. L. Mensa, High Resolution Radar Imaging, Artech House, Dedham, MA, 1982.
6. W. F. Gabriel, "Spectral Analysis and Adaptive Array Superresolution Techniques," Proc. IEEE, Vol. 68, pp. 654-666, Jun 1980.
7. J. Capon, "High-Resolution Frequency-Wavenumber Spectrum Analysis," Proc. IEEE, Vol. 57, pp. 1408-1418, Aug 1969.
8. R.O. Schmidt and R.F. Franks, "Multiple Source DF Signal Processing: An Experimental System," IEEE Trans. AP, Vol. 34, pp. 281-290, Mar 1986.
9. W.F. Gabriel, "Using Spectral Estimation Techniques in Adaptive Processing Antenna Systems," IEEE Trans. Antennas and Propagation, Vol. AP-34, pp. 291-300, Mar 1986.
10. J. T. Mayhan and L. Niro, "Spatial Spectral Estimation Using Multiple Beam Antennas," IEEE Trans. Antennas and Propagation, Vol AP-35, pp. 897-906, August 1987.
11. J. E. Evans, J. R. Johnson, and D. F. Sun, "Applicaton of Advanced Signal Processing Techniques to Angle of Arrival Estimation in ATC Navigation and Surveillance Sytems," MIT Lincoln Laboratory Tech. Report 582, (FAA-RD-82-42), June 1982.
12. B. D. Steinberg, "Microwave Imaging of Aircraft," Proc. IEEE, Vol. 76, pp 1578-1592, Dec. 1988.
13. M. Skolnik, Radar Handbook, McGraw-Hill Book Co., NY, 1970
14. R.A. Monzingo and T.W. Miller, "Introduction to Adaptive Arrays," Wiley, NY, 1980

15. A.V. Oppenheim and R.W. Schafer, Digital Signal Processing, Prentice Hall, Englewood Cliffs, NJ, 1975.
16. J. Butler, "Multiple Beam Antennas," Sanders Assoc. Internal Memo RF 3849, Jan 1960.
17. S.P. Applebaum, "Adaptive Arrays," IEEE Trans. Antennas and Propagation, Vol. AP-24, pp. 585-598, Sep 1976.
18. W.F. Gabriel, "Building Block for an Orthornormal-Lattice-Filter Adaptive Network," NRL Report 8409, July 1980.
19. W.F. Gabriel, "Large-Aperture Sparse Array Antenna Systems of Moderate Bandwidth for Multiple Emitter Location," IEEE Trans/ Antenna and Propagation, Vol. 37, No. 1, pp. 16-29, Jan 1989..
20. N.J. Nilsson, "On the optimum range resolution of radar signals in noise," IRE Trans. Inform. Theory, vol. IT-11, pp. 245-253, 1961.
21. W.L. Root, "Radar resolution of closely spaced targets," IRE Trans. Mil. Electron., vol. MIL-6, pp. 197-204, 1962.
22. M.G. Lichtenstein and T.Y. Young, "The resolution of closely spaced signals," IEEE Trans. Inform. Theory, vol. IT-14, pp. 288-293, 1968.
23. D.G. Childres, R.S. Varga, and N.W. Perry, "Composite signal decomposition," IEEE Trans. Audio Electroacoust., vol. AU-18, pp. 471-475, 1970.
24. J.E. Ehrnberg, T.E. Edwart, and R.D. Morris, "Signal processing techniques for resolving individual pulses in a multipath signal," J. Acoust. Soc. Amer., vol. 63, pp. 1861-1865, 1978.
25. R.J.P. Figueiredo and A. Gerber, "Separation of superimposed signals by a cross correlation method," IEEE Trans. Acoust., Speech, Signal Processing, vol. ASSP-31, pp. 1084-1089, 1983.
26. A.M. Bruckstein, T.J. Shan, and T. Kailath, "The Resolution of Overlapping Echos," IEEE Trans. ASSP, Vol. 33, pp. 1357-1367, Dec. 1985.
27. E.K. Walton, "Comparison of Fourier and Maximum Entropy Techniques for High-resolution Scattering Studies", Radio Science, Vol. 22, No.3, pp. 350-356, May 1987.
28. R.T. Compton, Jr., "Two-dimensional Imaging of Radar Targets with the MUSIC Algorithm," Ohio State Univ. Technical Report 719267-14, Dec. 1987.
29. T.J. Shan and T. Kailath, "Adaptive Beamforming for Coherent Signals and Interference," IEEE Trans. on Acoustics, Speech and Signal Processing, vol. ASSP-33, no. 3 (June 1985), p. 527-536.
30. R.O. Schmidt, "Multiple Emitter Location and Signal Parameter Estimation," IEEE Trans. Antennas and Propagation, Vol. AP-34, pp 276-280, Mar. 1986.

TABLE 1

ROTATING-BOOM MODEL for SIMULATED DATA

$f_r=0.63$ rpm, prf=418 Rangebin=31.25 λ $\theta=90$ deg. at $t=0$

Target No.	SNR in dB	Distance d_i	Doppler in Hz.	Doppler in %prf	Doppler in deg.
1	0	+45.0	-185.6	-44.4	-159.8
2	0	+30.0	-123.7	-29.6	-106.5
3	0	+19.0	-78.3	-18.7	-67.5
4	23	+10.0	-41.2	-9.9	-35.5
5	23	+9.2	-37.9	-9.1	-32.7
6	23	+1.6	-6.5	-1.6	-5.6
7	23	+0.8	-3.3	-0.8	-2.8
8	23	0.0	0.0	0.0	0.0
9	0	-5.1	+20.9	+5.0	+18.0
10	20	-6.8	+27.8	+6.7	+24.0
11	10	-8.4	+34.8	+8.3	+30.0
12	20	-10.1	+41.8	+10.0	+36.0
13	0	-19.0	+78.3	+18.7	+67.5
14	0	-30.0	+123.7	+29.6	+106.5
15	0	-45.0	+185.6	+44.4	+159.8

TABLE 2

ROTATING-BOOM MODEL for SIMULATED DATA

$f_r=0.1$ rpm, prf=200, Rangebin=150 λ , $\theta=45$ deg. at $t=0$

Target No.	SNR in dB	Distance d_i	Doppler in Hz.	Doppler in %prf	Doppler in deg.
1	10	+1.0	-3.78	-1.89	-6.81
2	10	0.0	-1.56	-0.78	-2.81
3	10	-1.0	+0.66	+0.33	+1.19

Note: Doppler offset of -1.5625 Hz., all three targets.

TABLE 3

ROTATING-TRIANGLE MODEL, TEN POINT-TARGETS

TARGET No.	SNR IN DB	RADIUS D_1	ANGLE θ_1	DOPPLER IN HZ	DOPPLER IN %PRF	DOPPLER IN DEGREES
1	0.0	2.83	30.52	-6.07	-3.04	-10.94
2	3.5	1.48	30.52	-3.92	-1.96	- 7.06
3	7.0	0.492	30.52	-2.34	-1.17	- 4.22
4	10.0	0.0	0.0	-1.56	-0.78	- 2.81
5	7.0	0.87	-59.48	+0.79	+0.40	+ 1.43
6	3.5	2.03	-59.48	+3.93	+1.97	+ 7.08
7	0.0	2.83	-59.48	+6.09	+3.05	+10.97
8	0.0	2.24	-41.1	+3.06	+1.53	+ 5.51
9	0.0	2.00	-14.48	0.0	0.0	0.0
10	0.0	2.24	12.12	-3.04	-1.52	- 5.47

$f_r = 0.1$ rpm, prf= 200, Rangebin= 150 wavelengths, $t = 0$ start time,
Doppler offset of -1.5625 Hz. all ten targets.

TABLE 4

ROTATING-TRIANGLE MODEL, TEN POINT-TARGETS

TARGET No.	SNR IN DB	RADIUS D_i	ANGLE θ_i	DOPPLER IN HZ	DOPPLER IN %PRF	DOPPLER IN DEGREES
1	0.0	2.83	45.0	-7.86	-3.93	-14.15
2	3.5	1.41	45.0	-4.70	-2.35	- 8.46
3	7.0	0.70	45.0	-3.11	-1.55	- 5.60
4	10.0	0.0	0.0	-1.56	-0.78	- 2.81
5	7.0	0.71	-45.0	0.02	+0.01	+ 0.03
6	3.5	1.41	-45.0	+1.58	+0.79	+ 2.84
7	0.0	2.83	-45.0	+4.74	+2.37	+ 8.52
8	0.0	2.24	-26.6	+1.58	+0.79	+ 2.86
9	0.0	2.00	0.0	-1.56	-0.78	- 2.81
10	0.0	2.24	26.6	-4.71	-2.35	- 8.48

$f_r = 0.1$ rpm, prf= 200, Rangebin= 150 wavelengths, $t = 0$ start time,
Doppler offset of -1.5625 Hz. all ten targets.

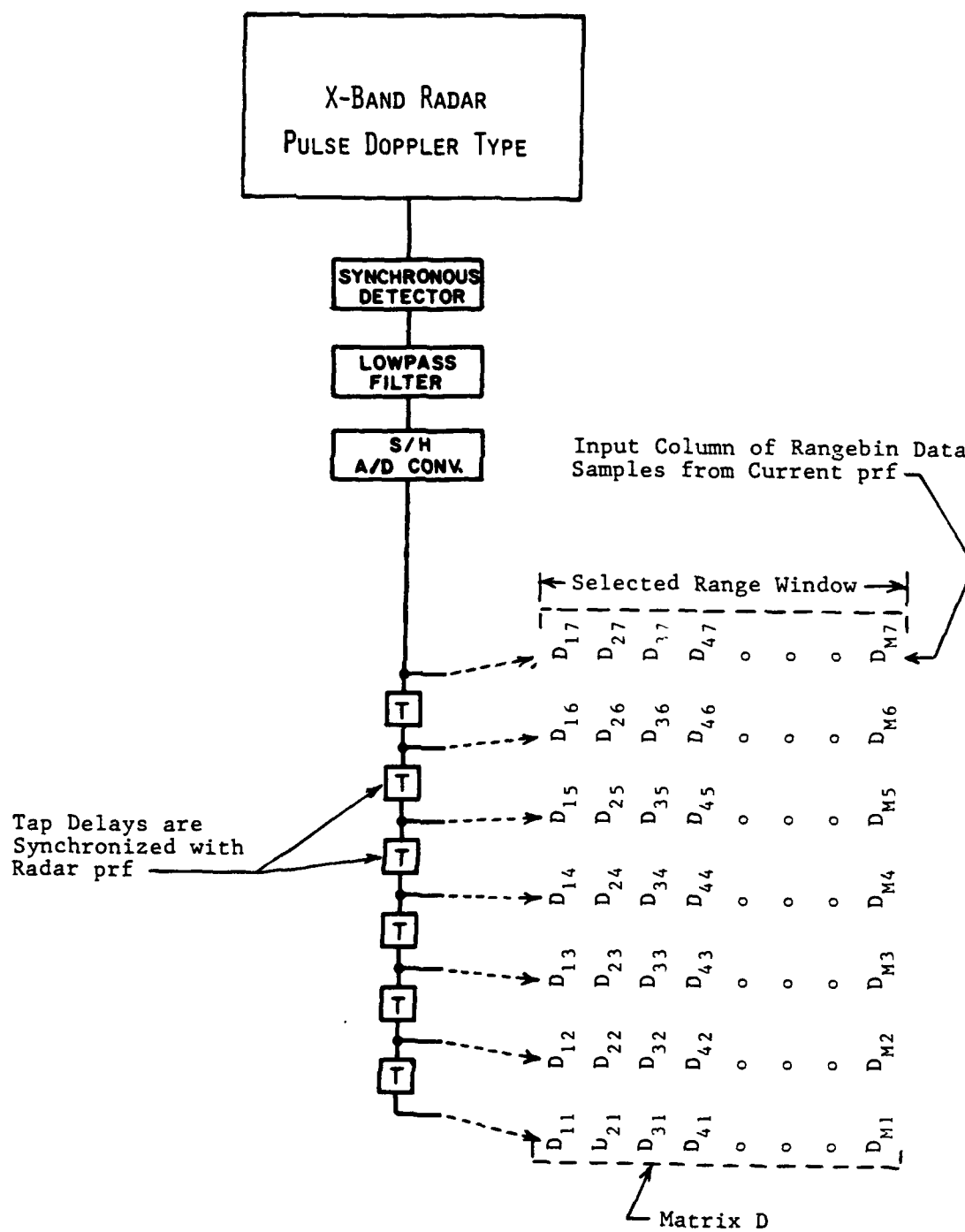


Fig. 1 — Simplified block diagram configuration to illustrate the matrix of synchronized data samples utilized for Doppler domain processing

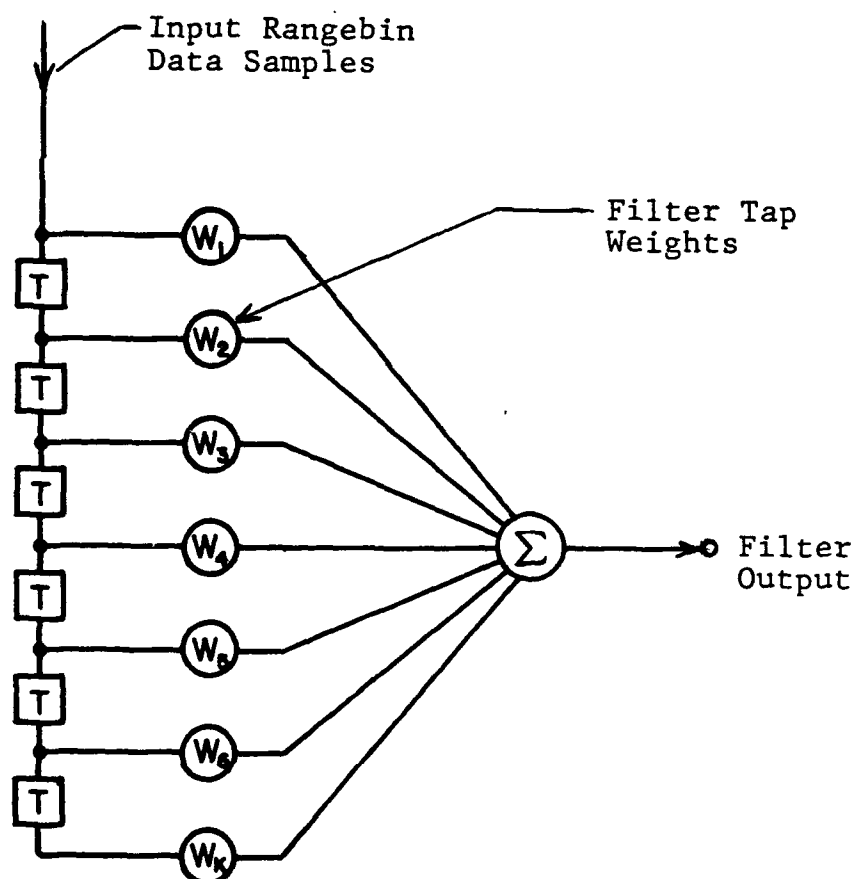


Fig. 2 — DFT transversal filter schematic; a weighted "beamformer" in the Doppler domain

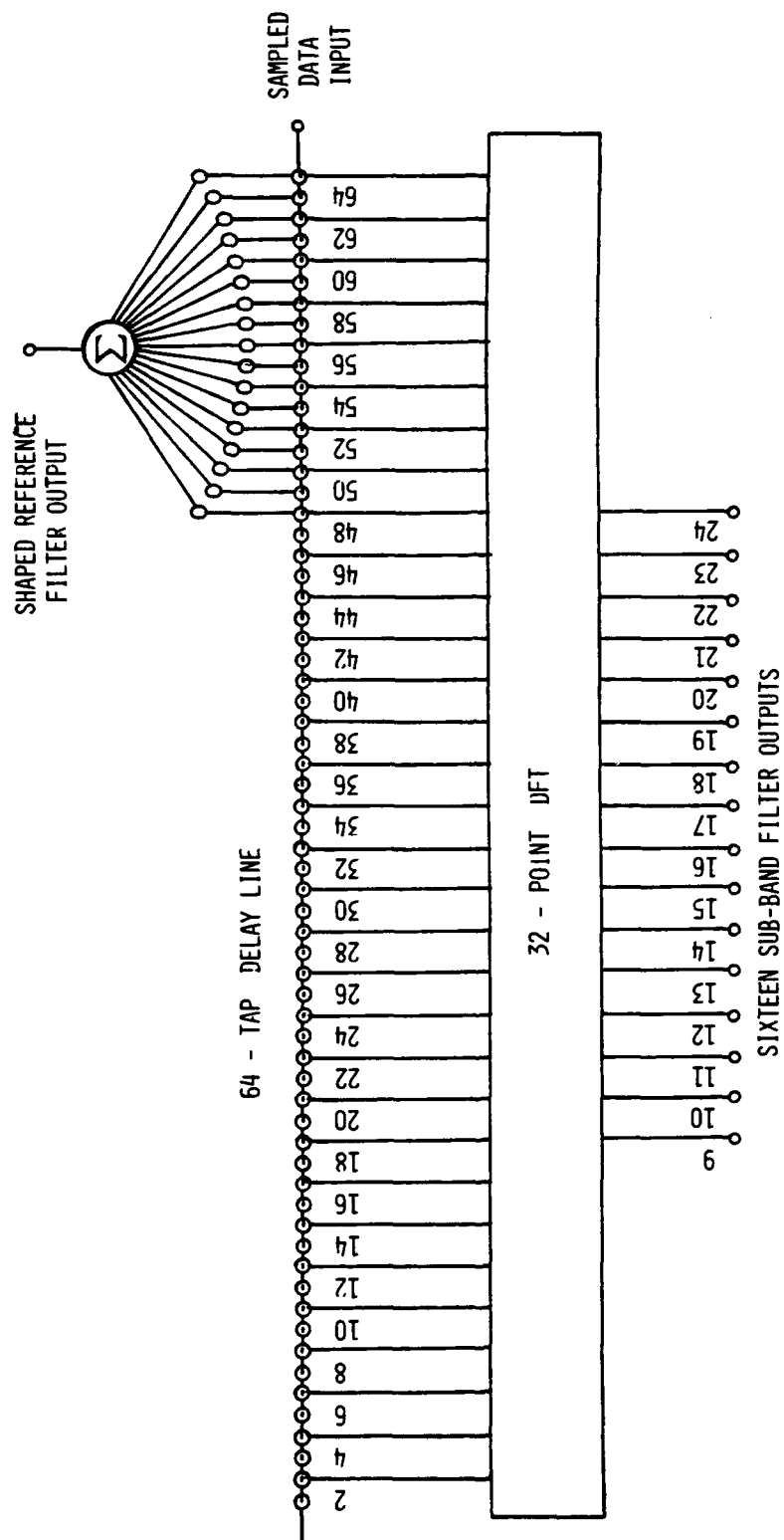


Fig. 3 — Time domain Doppler processor implementation of the "beam-space" LPP high-resolution algorithm

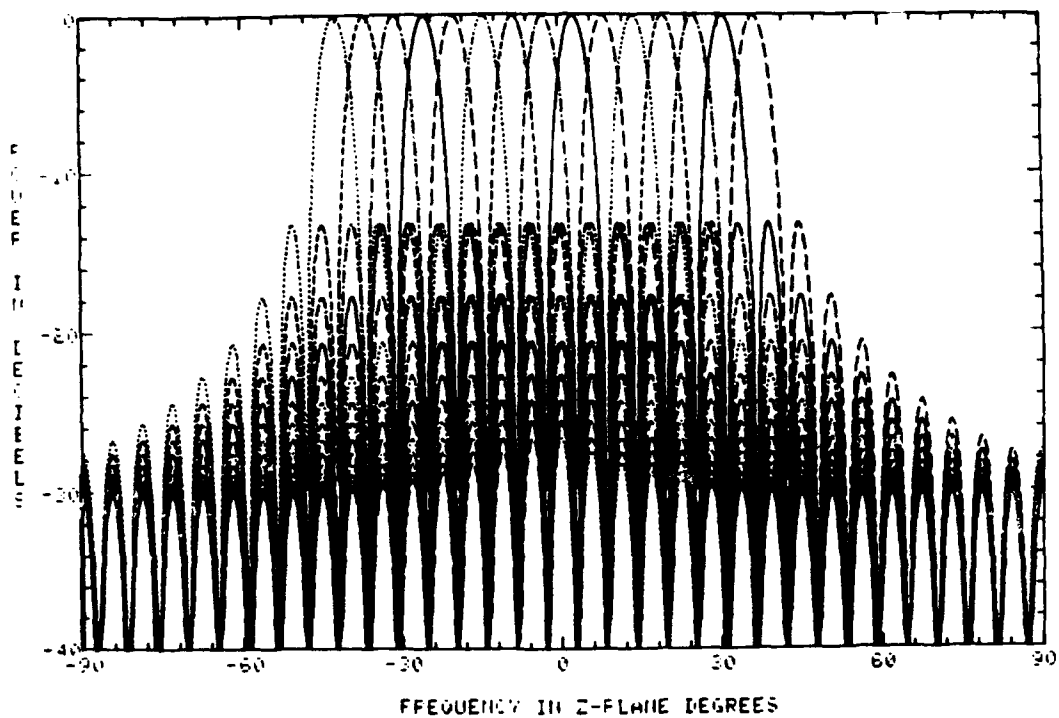


Fig. 4 — Multiple sub-bands selected from DFT which connects into the even-numbered taps along the 64-tap delay line

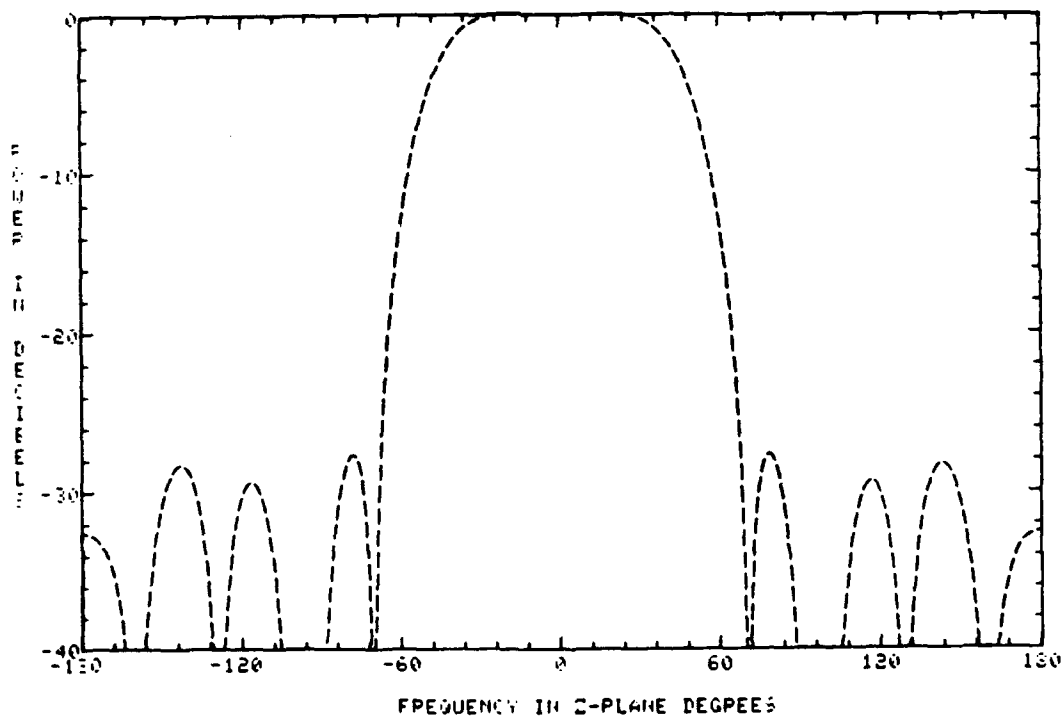


Fig. 5 — Reference Filter passband, 17 adjacent taps Nos. 48 thru 64

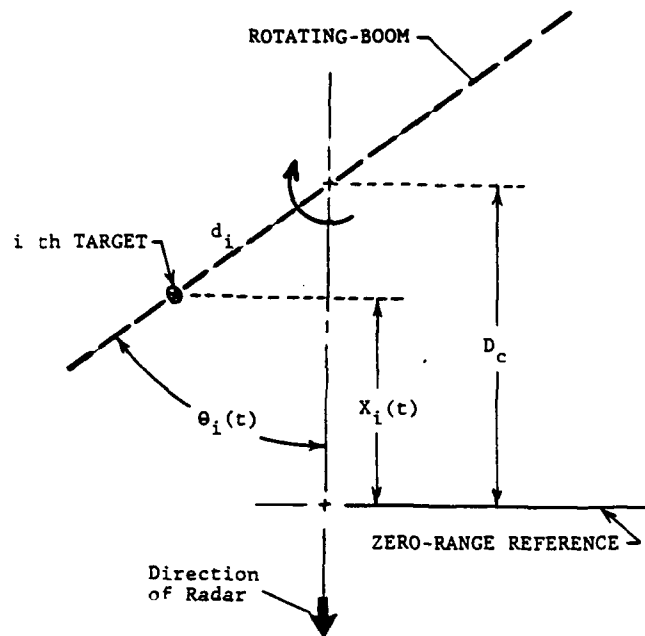


Fig. 6 — Rotating-boom along which are located point-targets, utilized for generating simulated radar data samples

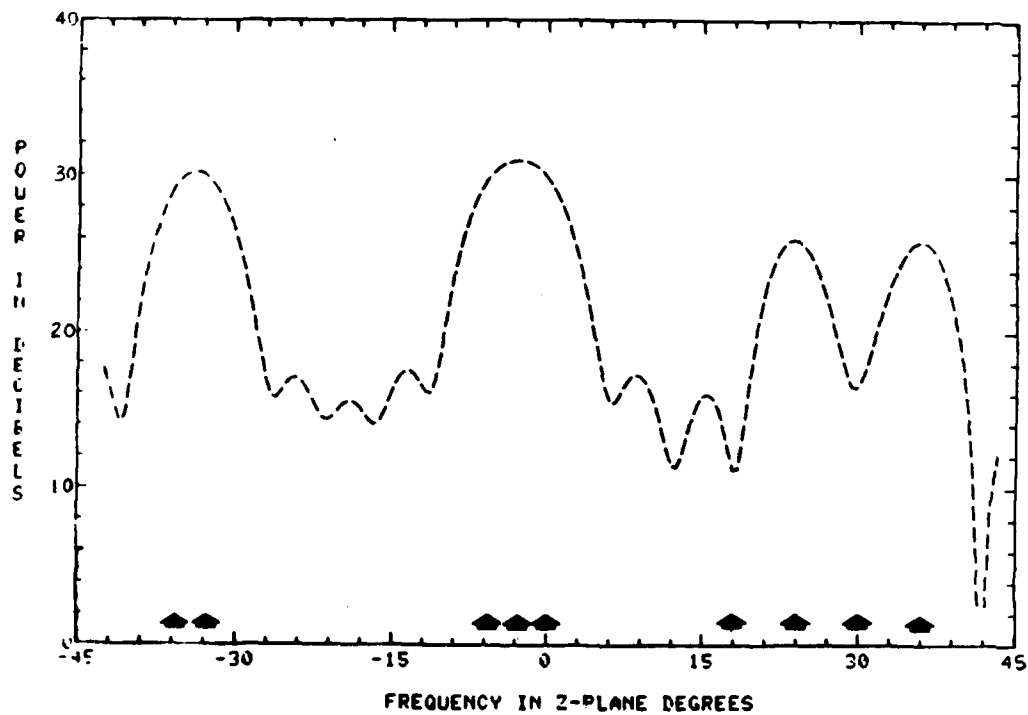
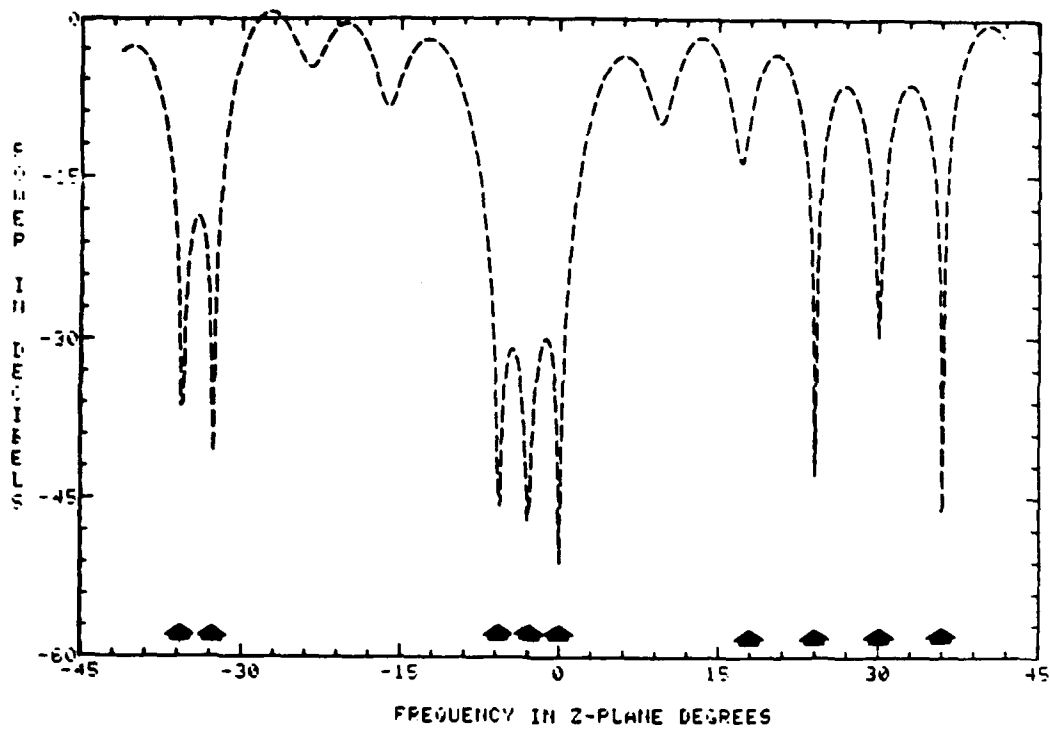
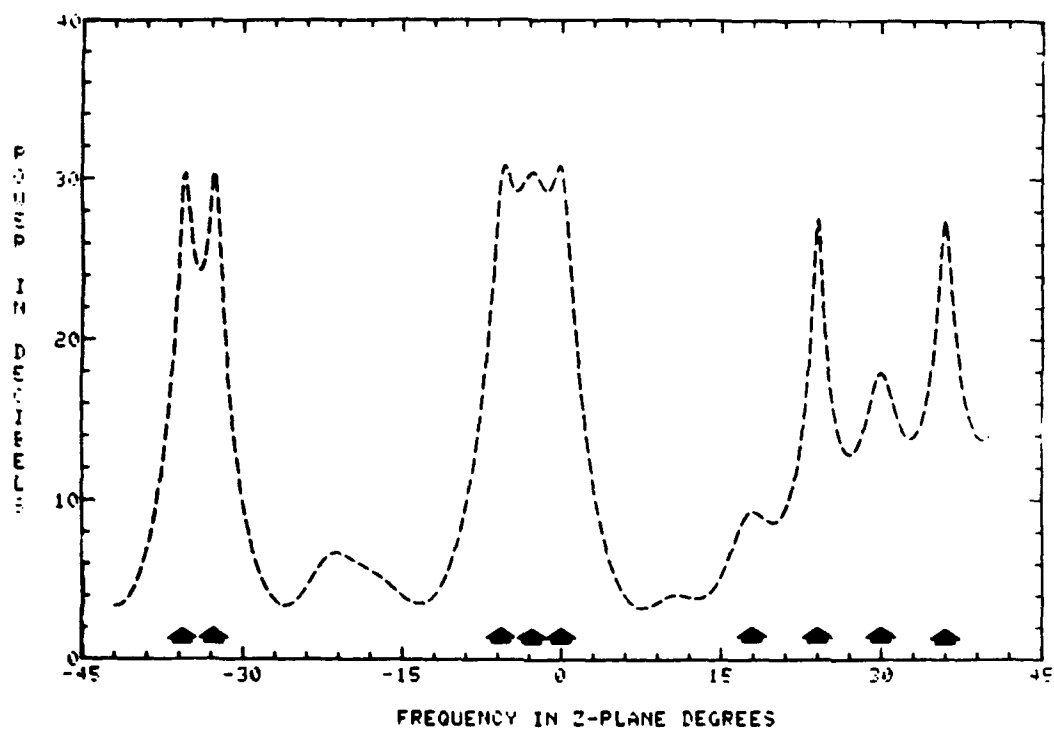


Fig. 7 — (a) Conventional Fourier transform



(b) Sub-band LPF Algorithm.



(c) Sub-band MLM Algorithm.

Fig. 7 — Typical spectrum estimates for nine sinusoids within passband; the five on the left are 23 dB; the four on the right are 0, 20, 10 and 20 dB signal-to-noise ratio. 140 data samples processed

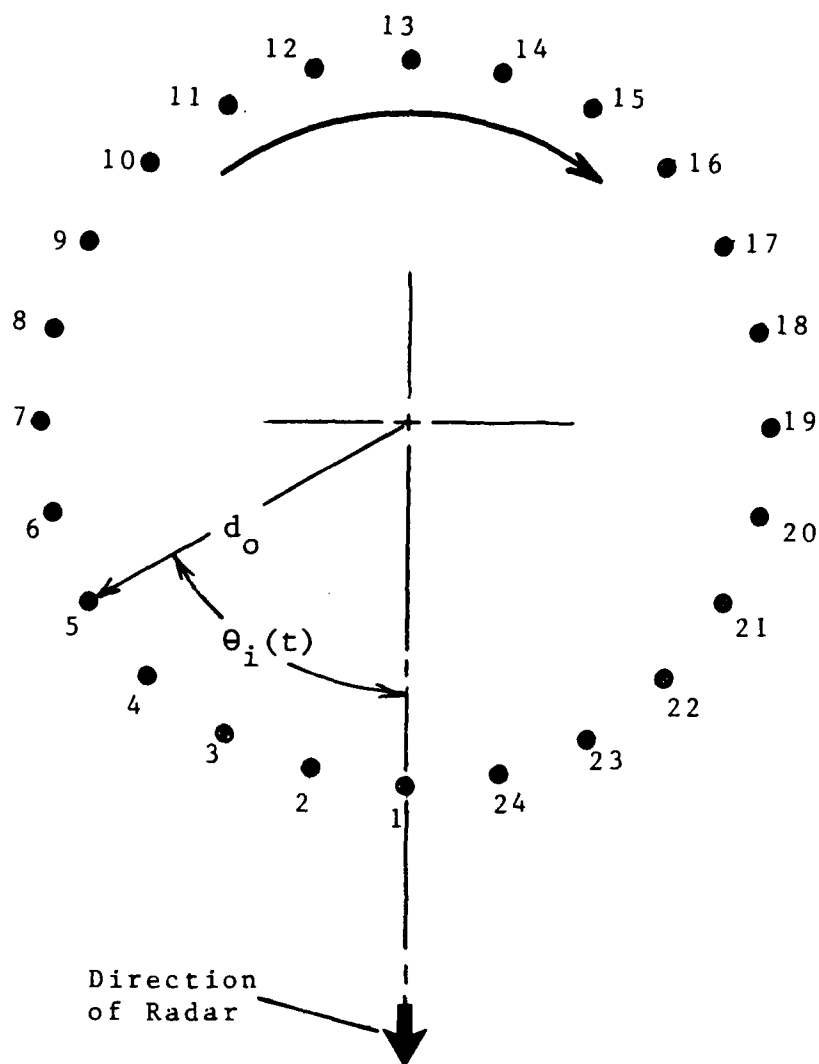
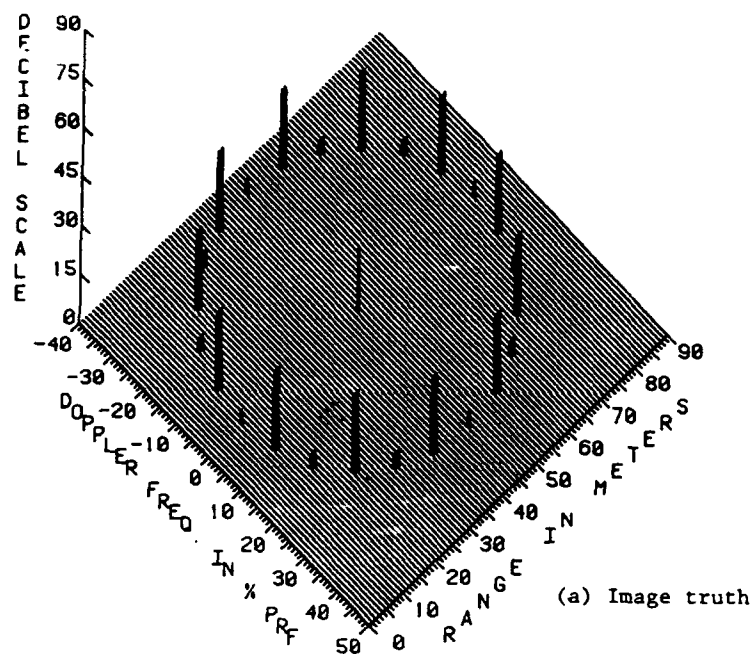
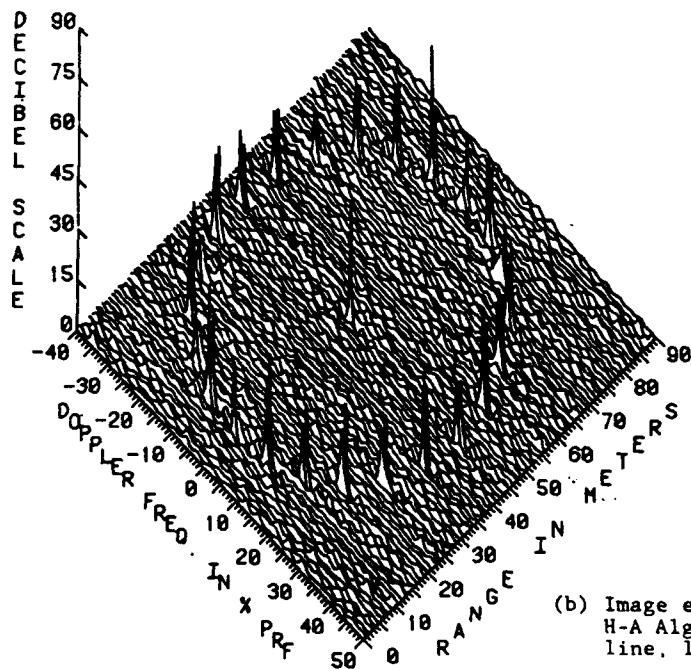


Fig. 8 — "Merry-Go-Round" of point-targets (24) equally spaced, utilized for generating simulated radar data samples

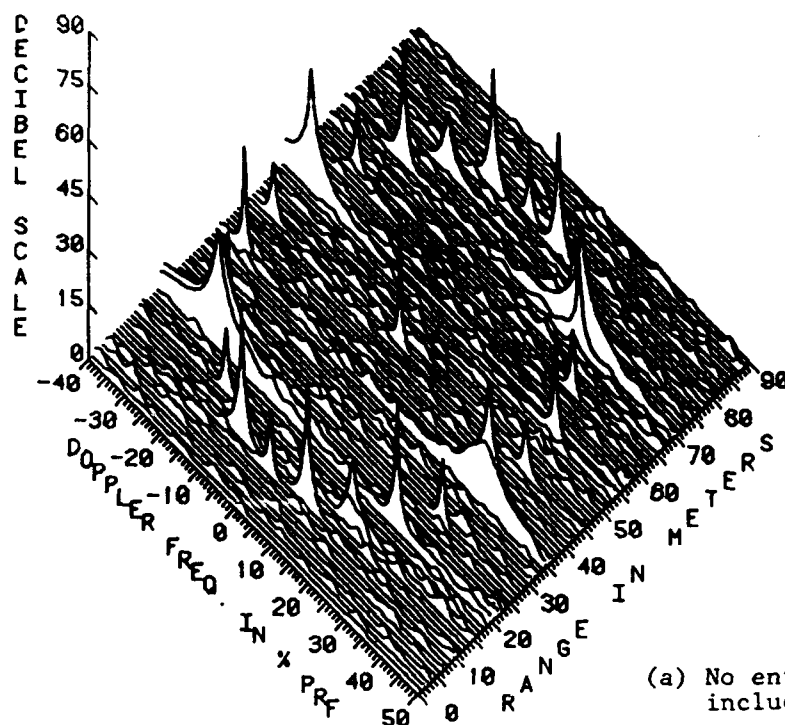


(a) Image truth

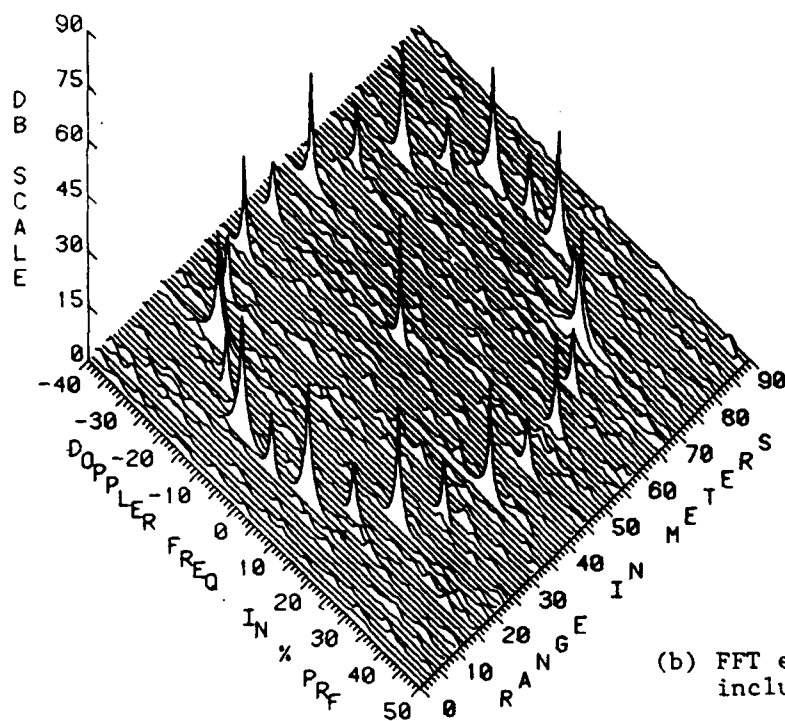


(b) Image estimate processed per H-A Algorithm, 32 tap delay line, 140 prf processed.

Fig. 9 — 3D Range-Doppler radar image of the rotating object. Simulation "Merry-Go-Round" of 24 equi-spaced point-targets, 35 m radius, and 0.63 rpm.



(a) No entry/exit routine included.



(b) FFT entry/exit routine included in processing.

Fig. 10 — 3D ISAR images of "Merry-Go-Round" rotating object, processed per MLM Algorithm, 32 tap delay line, 100 prf processed

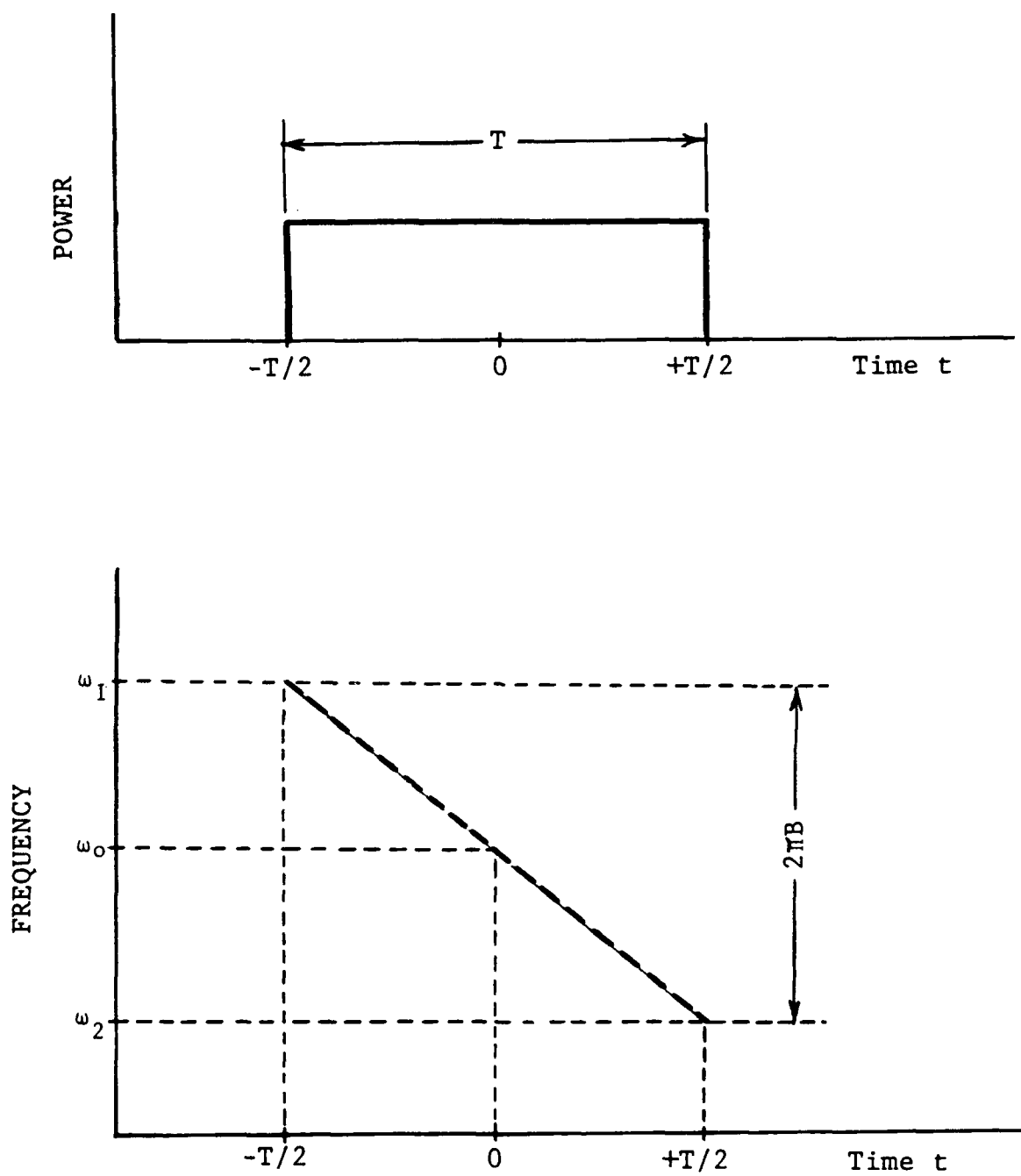
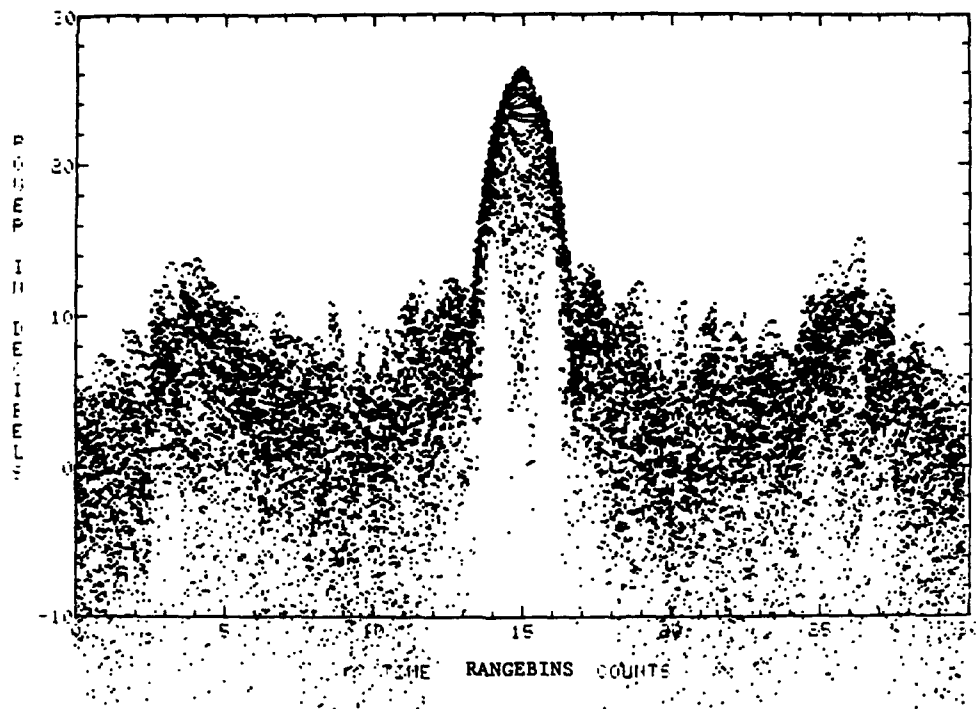
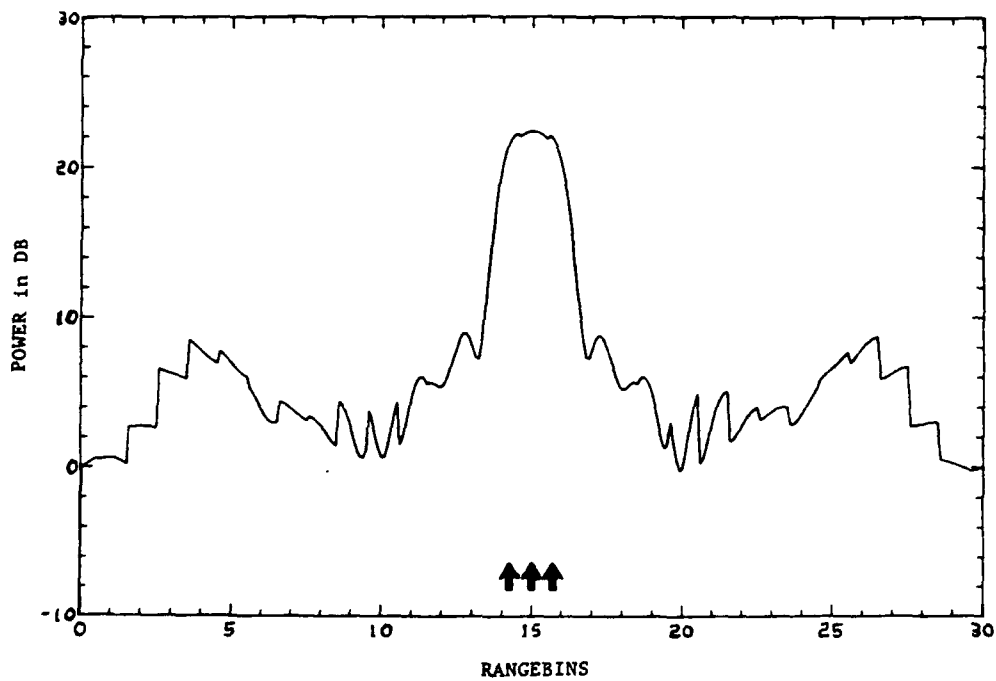


Fig. 11 — Linear FM chirp pulse, radar signal waveform

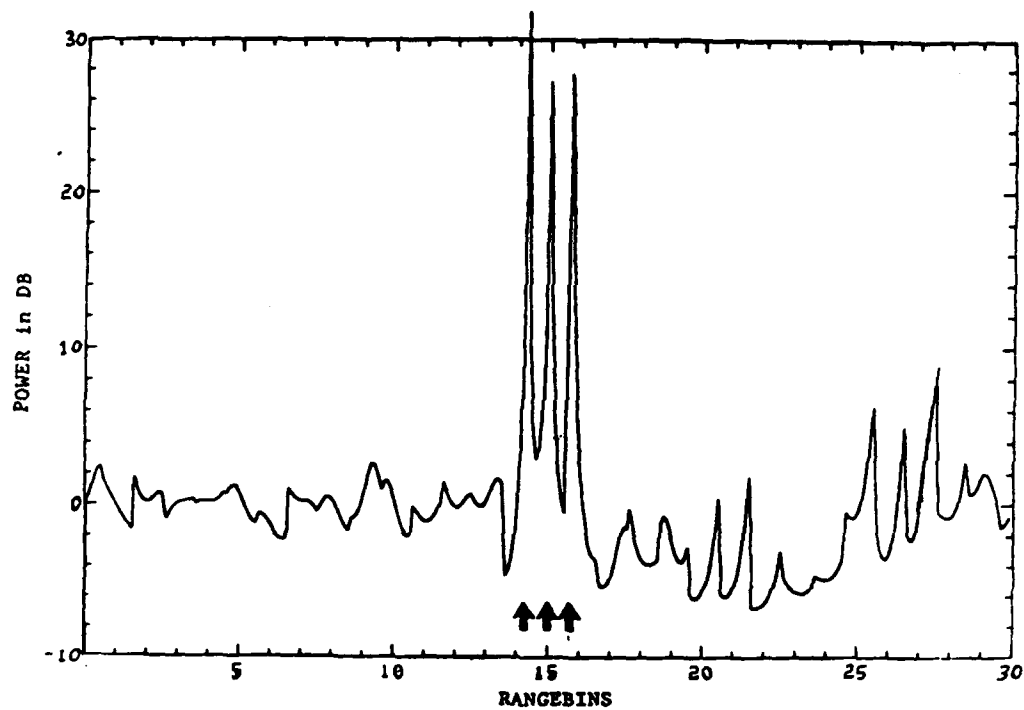


(a) Typical DFT output sequences, overlay plots

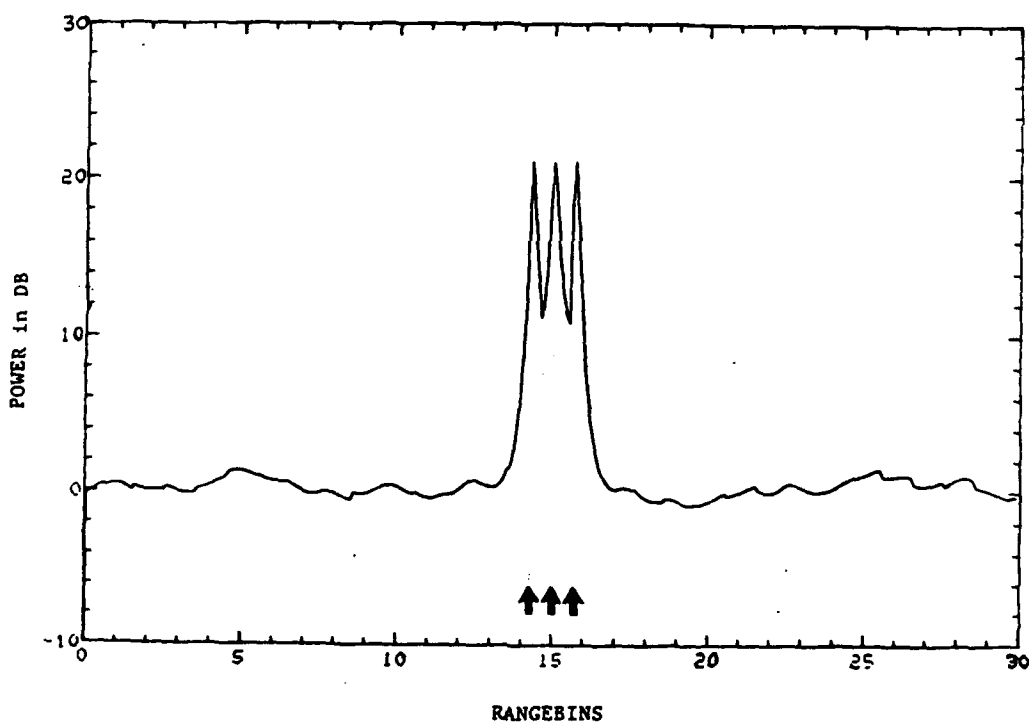


(b) DFT averaged over 264 prf.

Fig. 12 — Conventional DFT matched filter response for three-target case of Table 2



(a) Weiner SLC Algorithm optimum weight.



(b) MLM Algorithm

Fig. 13 — Target range estimate plots obtained from two high-resolution algorithms, 264 prf processed

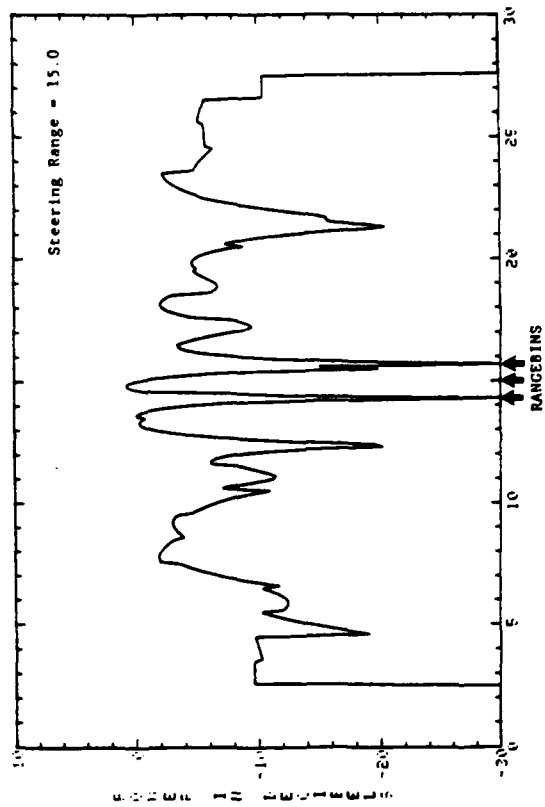
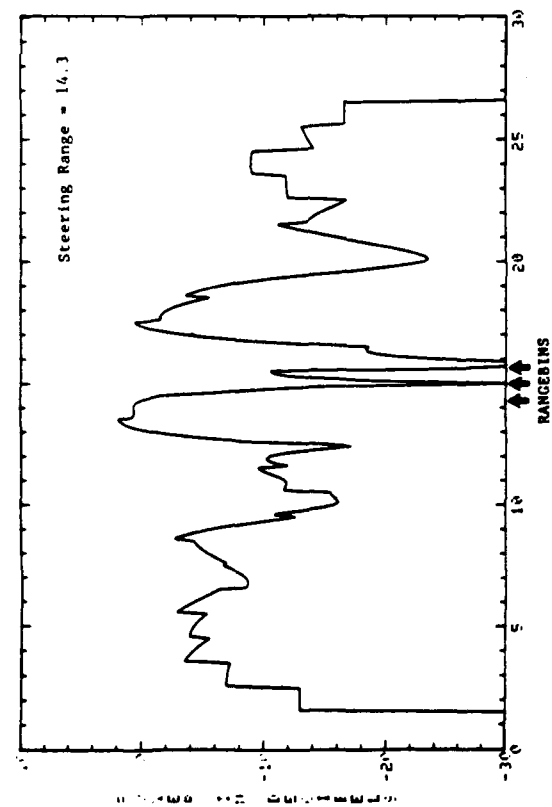
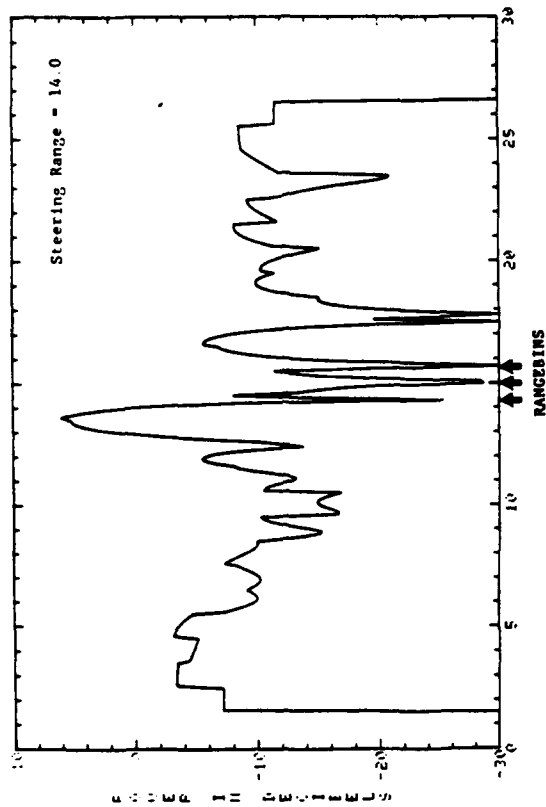
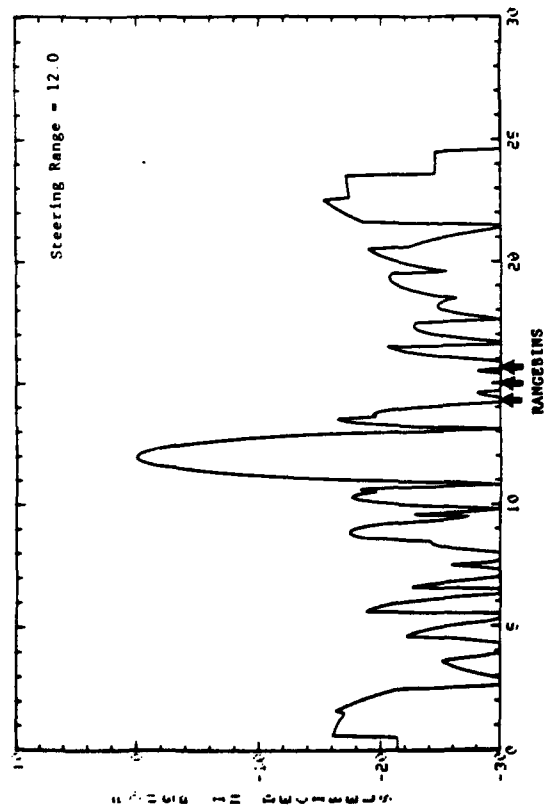
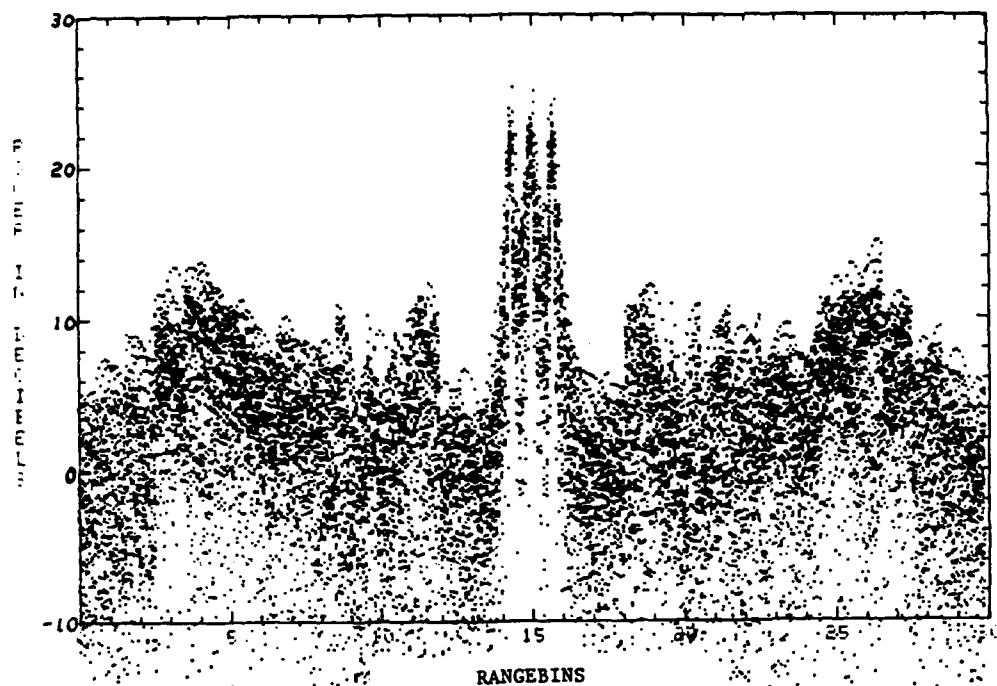
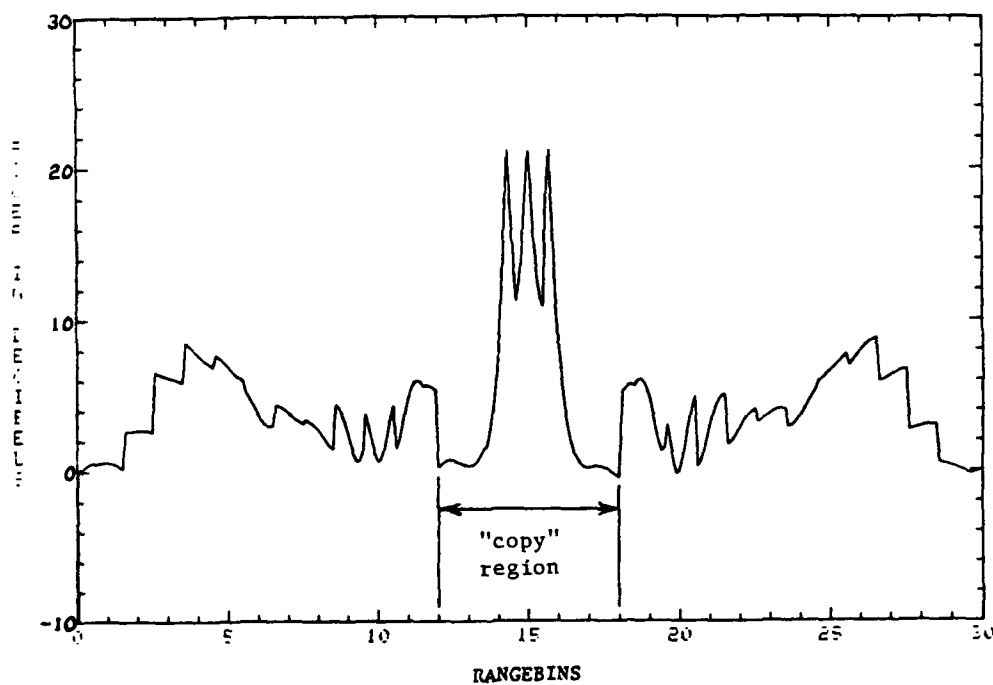


Fig. 14 — MLM "Copy" weight response in range domain for various "steering" range selections, three point-target case of Table 2



(a) Typical MLM "copy" weights output sequences.



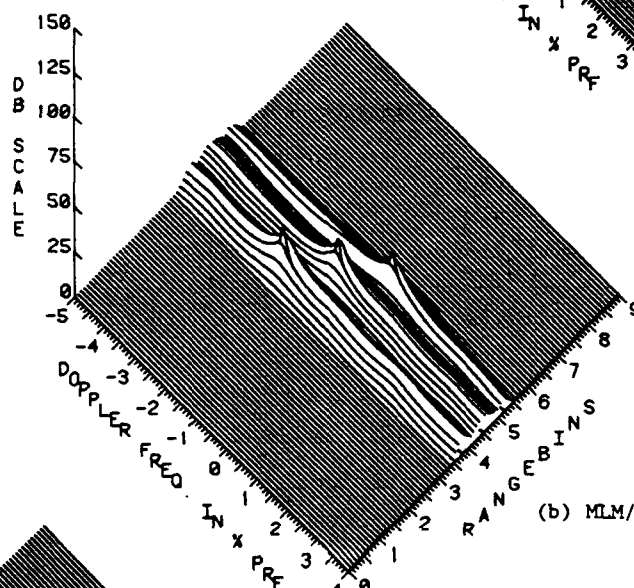
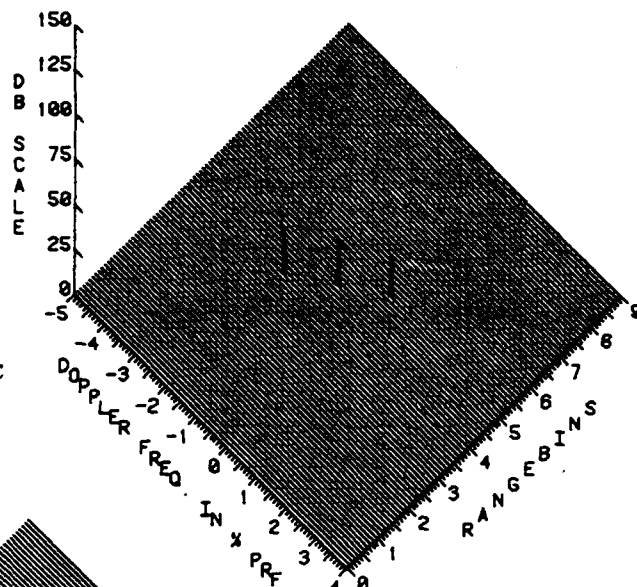
(b) MLM Algorithm outputs averaged over 264 prf.

Fig. 15 — MLM Algorithm "Copy" weights filter response, as applied to the rangebin region from 12.0 to 18.0

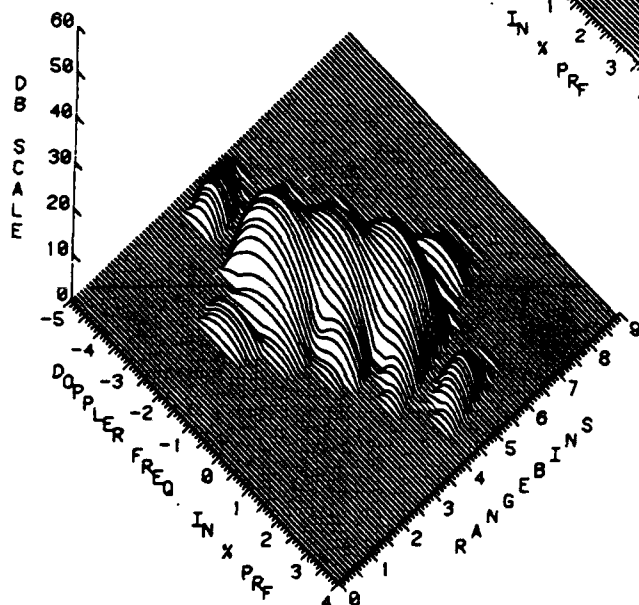
Chirp Pulse, Compression Ratio 13
64-Tap Delay Line, DFT Sub-Bands
264 PRF Processed

Three 10 DB Targets, 0.1 rpm
0.7 Rangebin-Dopplerbin Spacing

(a) Digital plot from Weiner SLC
Optimum Weight Roots



(b) MLM/LPF Algorithm, Shaped Filter



(c) Conventional Fourier Transform,
Rectangle Window, 15 DB threshold

Fig. 16 — Radar images of rotating object, three point-targets along rotating boom, Table 2 case

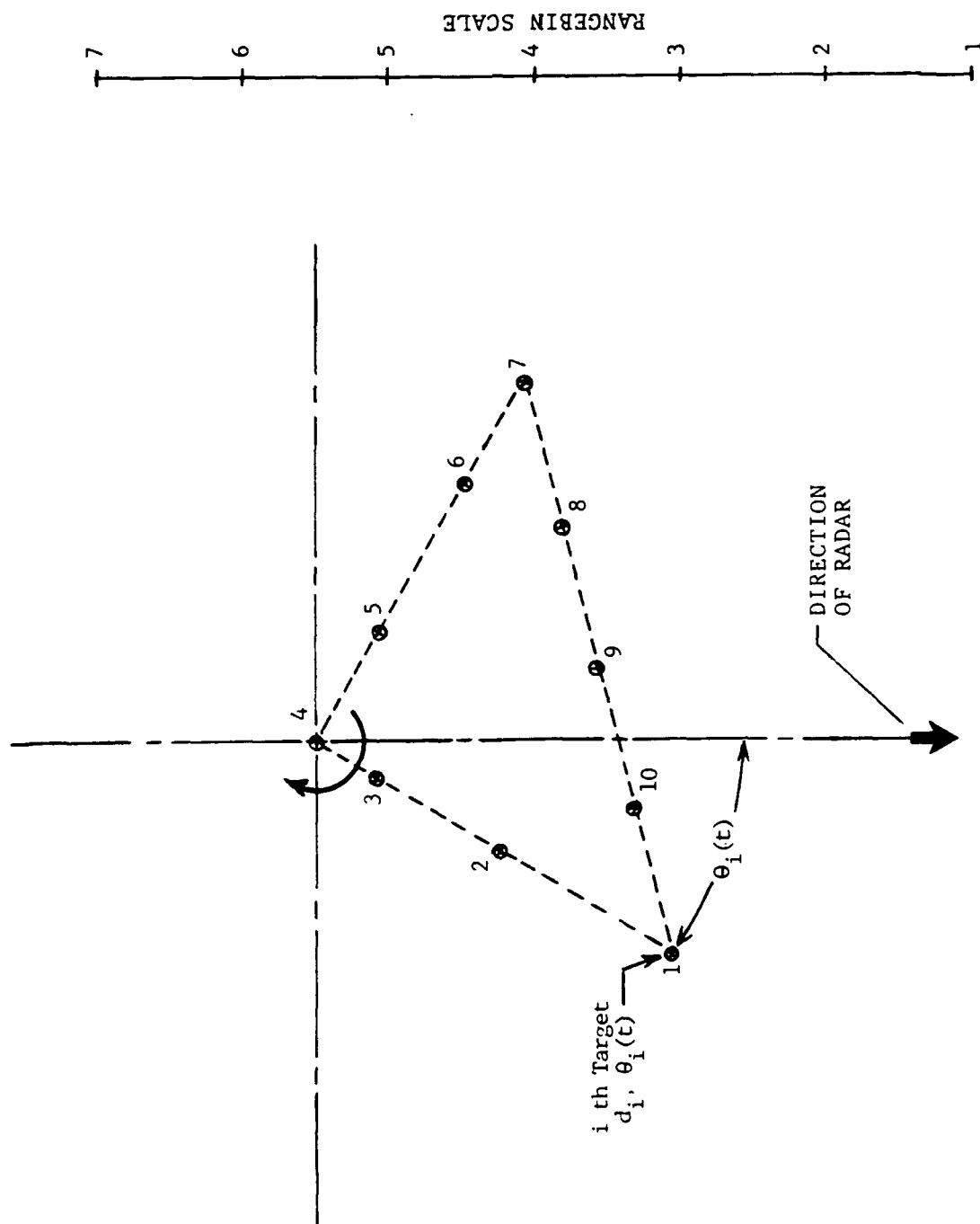


Fig. 17 — Rotating object consisting of ten point-targets arranged in the shape of a triangle

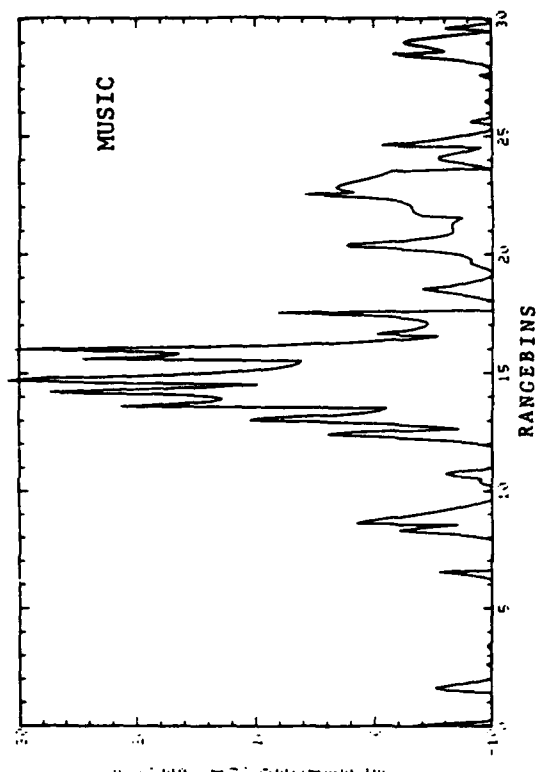
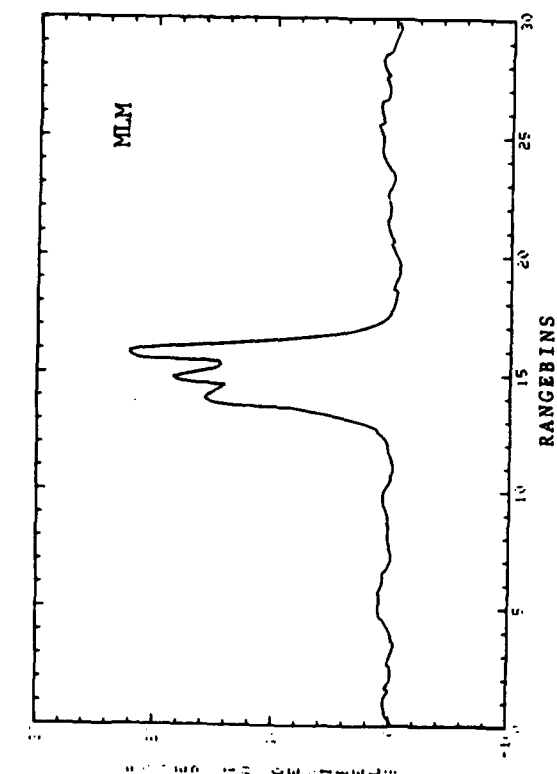
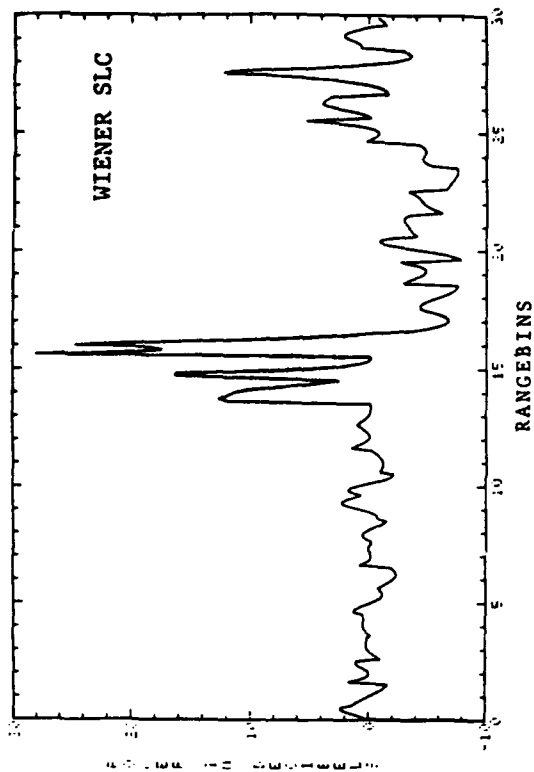
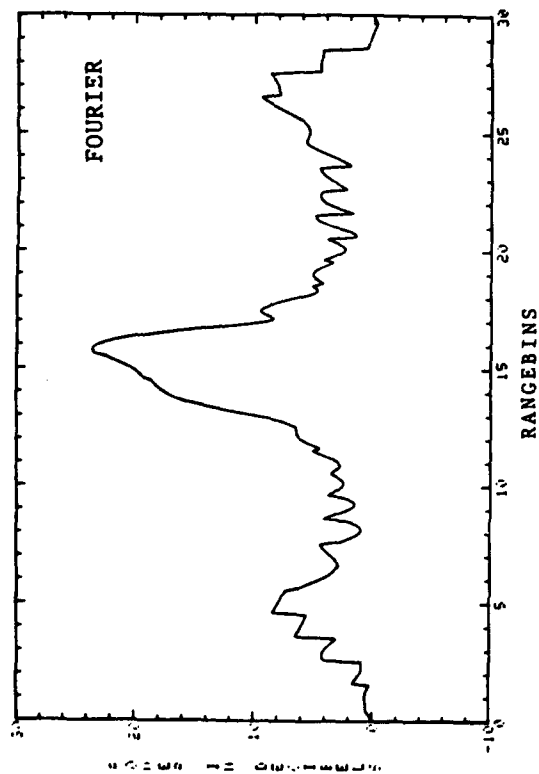
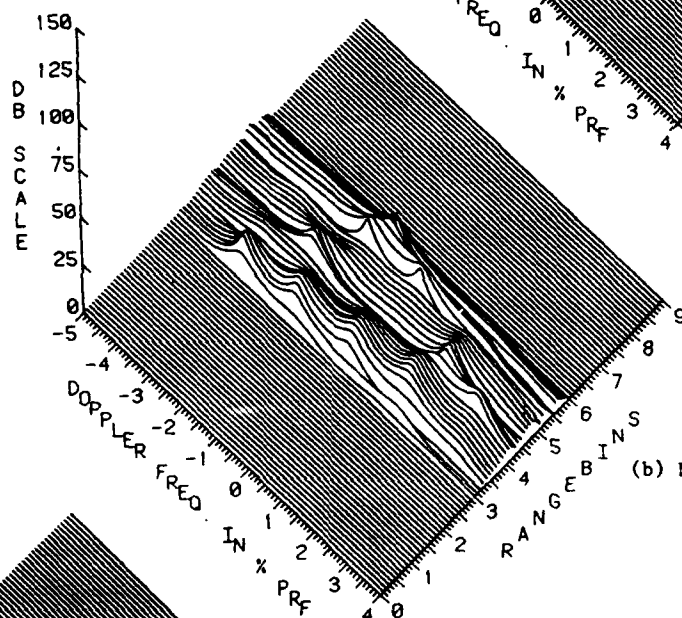
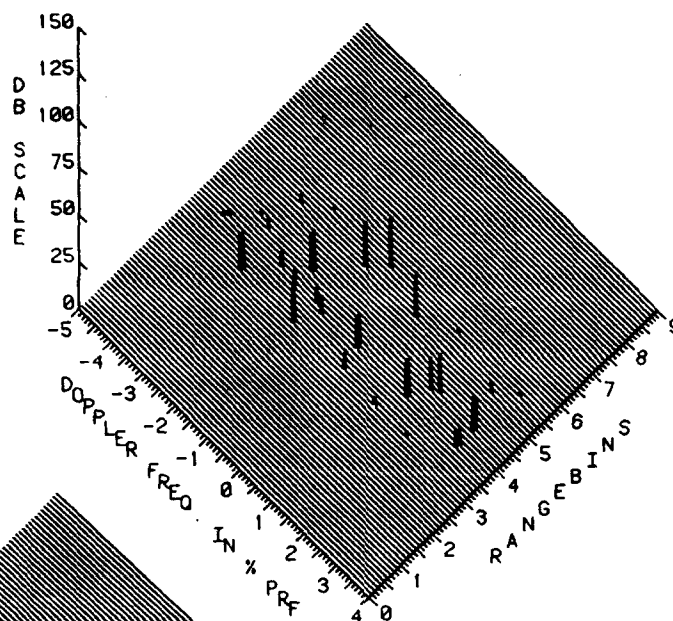
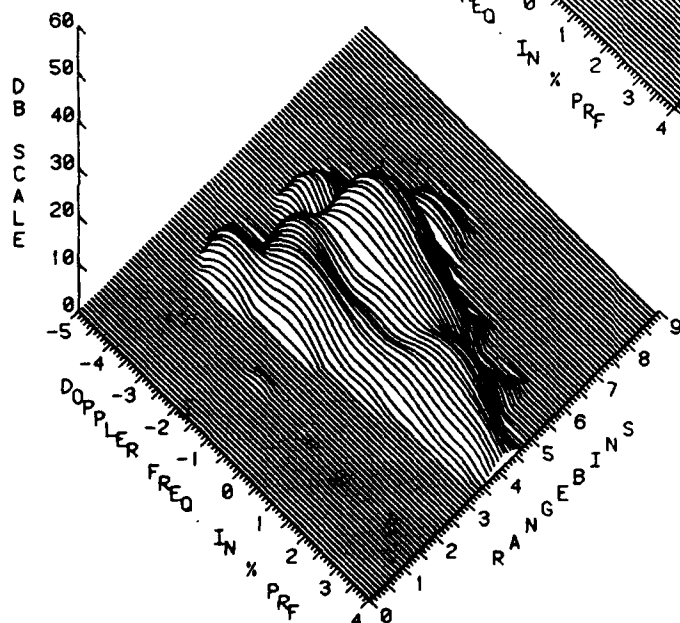


Fig. 18 — Range estimate plots for rotating-triangle model, ten point-targets, 264 prf processed

(a) Digital plot from Optimum Weight Roots.



(b) MLM Algorithm



(c) Conventional Fourier Transform,
Rectangle Window, 16 DB Threshold

Fig. 19 — Radar images of rotating object, ten point-targets in triangle shape, Table 3 case in which decorrelation is approximated

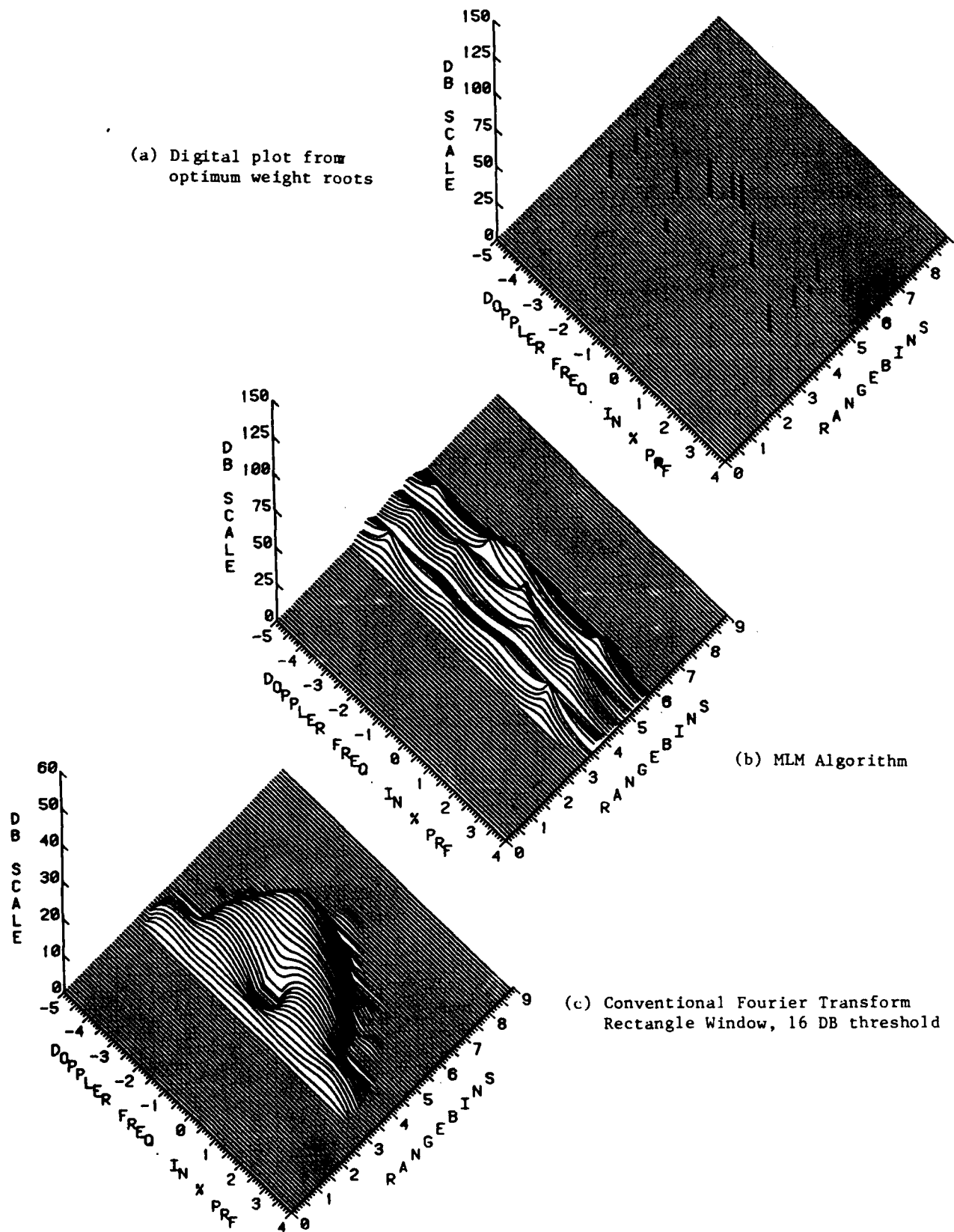


Fig. 20 — Radar images of rotating object, ten point-targets in triangle shape, Table 4 case in which three pairs are coherent